Available online at www.sciencedirect.com

ScienceDirect

Advances in Space Research 75 (2025) 542–559

ADVANCES IN SPACE RESEARCH
(a COSPAR publication)

www.elsevier.com/locate/asr

Analysis and interpretation of the in-flight dynamics of a critical space mechanism

Edoardo Dalla Ricca *, Daniele Bortoluzzi, Davide Vignotto

Department of Industrial Engineering, University of Trento, Trento 38123, Italy
National Institute for Nuclear Physics (INFN), Trento 38123, Italy

Received 26 January 2024; received in revised form 30 October 2024; accepted 15 November 2024
Available online 29 November 2024

Abstract

The study hereby presented develops a mechatronic model of a critical space mechanism for a comprehensive interpretation of its in-flight performance. The mechanism was operated in the LISA Pathfinder European Space Agency mission, which was flown to test key technologies developed for detecting gravitational waves from space. The mission accomplished its scientific goal, i.e. demonstrating that the noise level affecting the relative acceleration between two test masses is within the requirements. Even though LISA Pathfinder was a successful mission, some criticalities had to be overcome. The mechanism responsible for releasing the test masses into free-fall caused the masses to assume unexpected velocities. Preliminary analyses, based on a mixed experimental-analytical approach relying on planar dynamic models, demonstrated that the velocities could be explained by impacts between the test masses and the mechanism end-effectors. Starting from the results of these analyses, the study hereby presented develops a fully 3D electro-mechanical lumped-parameter model of the mechanism, following a completely analytical approach. The model, which is validated through an extensive experimental campaign, benefits from a coupled dynamics between the two critical planes and aims at a comprehensive description of the mechanism performance. The signal processing technique adopted to estimate the model parameters is based on a regression algorithm, simultaneously applied to multiple signals of the mechanism dynamic response. Then, a mathematical model of the test masses and of its impactive interactions with the mechanism end-effectors is developed to perform a full description of the in-flight dynamics of the release phase. The test mass telemetry signals are processed to estimate its state at the in-flight releases and compared with the prediction of the validated model, highlighting accordance with the in-flight data and giving a reliable interpretation of the anomalies in the test masses state.

Keywords: Mechanism model identification; Space mechanism testing; Mechanism micro vibration; Multiple signals simultaneous fit; LISA pathfinder

1. Introduction

LISA Pathfinder (LPF) is an European Space Agency mission that aimed at testing some fundamental technologies developed to be implemented in the first in-space gravitational waves observer, LISA (Armano et al., 2009). The LPF scientific payload included two gravitational reference sensors (GRS, Bortoluzzi et al., 2004; Armano et al., 2017; Dolesi et al., 2003), each one containing the sensing body of the experiments, a 1.928kg gold-coated cubic-shaped test mass (TM). Once the spacecraft reached the in-orbit phase, in order to start the scientific operations, the TMs had to be released into free-fall. This procedure was performed by the Grabbing Positioning and Release Mechanism (GPRM, Bortoluzzi et al., 2010; Mäusli et al., 2007; Neukom et al., 2009; Köker et al., 2013). The GPRM is

---

* Corresponding author at: Department of Industrial Engineering, University of Trento, Trento 38123, Italy.
E-mail address: edoardo.dallaricca@unitn.it (E. Dalla Ricca).

https://doi.org/10.1016/j.asr.2024.11.040
0273-1177/© 2024 COSPAR. Published by Elsevier B.V.

composed of two halves, located on two opposite sides of the TM (see Fig. 1a). On each half, a cylinder-shaped end effector named plunger is designed to grab the TM by fitting inside two pyramidal indents machined on two opposite TM faces. The shape of the plunger heads makes it possible to grab and center the TM from any possible configuration in the housing by commanding an axial displacement of the two opposed end effectors. A second actuator is located inside each plunger, to separate the TM from the plunger heads and perform the final release to free-fall, by means of an independent tip-shaped end effector. Given this design, the TM residual velocity after the release is expected to lay along the z-axis, i.e. the direction of retraction of the tips. Unexpectedly, the analysis of the in-flight telemetry data shows that all the TM velocity components were different from zero and non-compliant with the requirements along every direction, and that the z component was not the predominant one. Furthermore, the TM linear momentum after the releases laid almost totally on the x-z plane (Bortoluzzi et al., 2019; Bortoluzzi et al., 2021c; Schleicher et al., 2018).

Explaining what caused the unexpected releases is a non trivial task. Indeed, not all the in-flight releases which resulted non-compliant are reliable in terms of uncertainty on the estimation of the TM residual velocity components (Bortoluzzi et al., 2021c). Furthermore, the telemetry signals are available only for the TMs and no relevant data about the GPRMs state are present.

The main hypothesis formulated to explain the unexpected release velocities is that collisions between the plungers and the TM occurred at the tip retraction. This hypothesis is investigated in Bortoluzzi et al., 2021b, where a simple 2D model of the mechanism is developed and experimentally validated by means of interferometric measurements of its dynamical response at the tip retraction. The dynamical model is completed by an impact model between the plunger and the TM, predicting a TM kinetic energy compatible with that measured in the reliable in-flight releases. This dynamical model describes the mechanism dynamics only on the x–z plane, using a mixed experimental-analytical approach. In Bortoluzzi et al., 2021a, two similar lumped parameter plane models of the GPRM are presented, using a completely analytical approach. One model describes the GPRM dynamics on the x–z plane, the other one the mechanism response on the y–z plane. Even if this approach leads to promising results, it is affected by some drawbacks. First, no dynamic coupling is taken into account between the two planes. Second, the models' parameters are not estimated simultaneously, meaning that two different fitting procedures are executed, one for each plane. As a consequence, two different estimates of the same parameter are produced by the two in-plane models.

The analysis hereby presented aims at overcoming these limitations by means of the following improvements:

- a fully 3D model is developed using a completely analytical approach, and is exploited to reproduce the coupled dynamics on the two relevant planes,
- the 3D model is experimentally validated through an extensive ground-testing campaign,
- the model results are used to predict the TM state after a possible impact with the mechanism end effector, produced by the micro-metric vibration triggered by its activation. The comparison between the predicted and in-flight measured TM state at the release is performed to support the hypothesis.

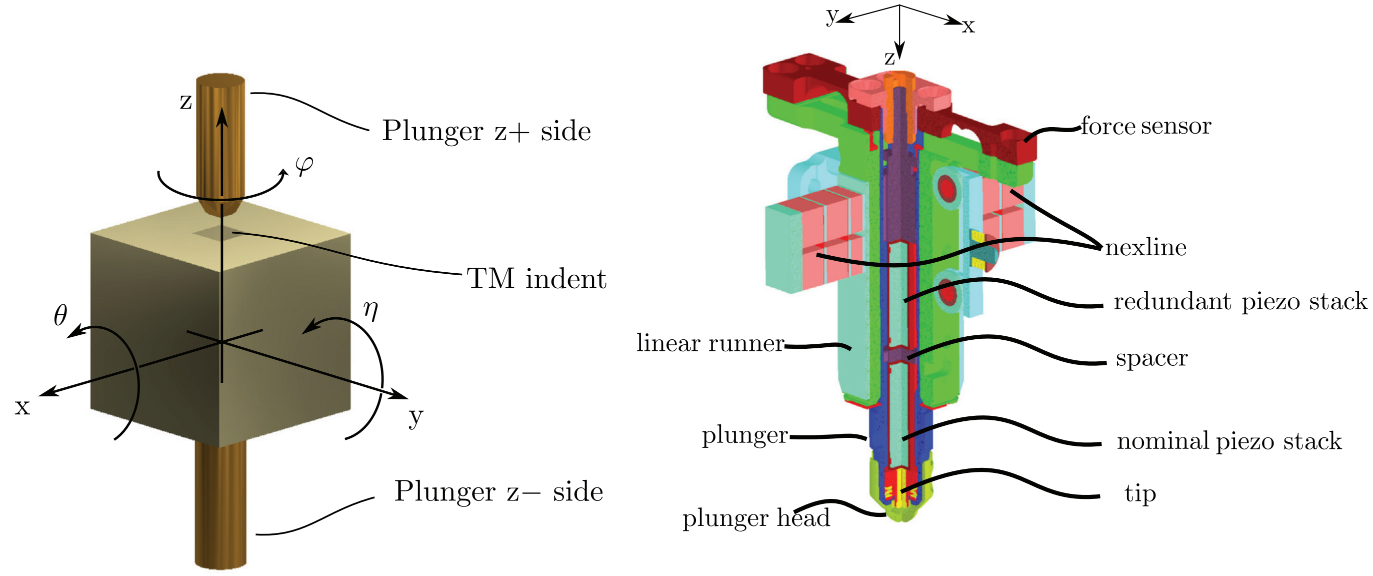

(a) (b)

Fig. 1. On the top left, rendering of the TM and the two plungers together with the reference frame describing the TM position and attitude. On the top right, section view of the mechanism.

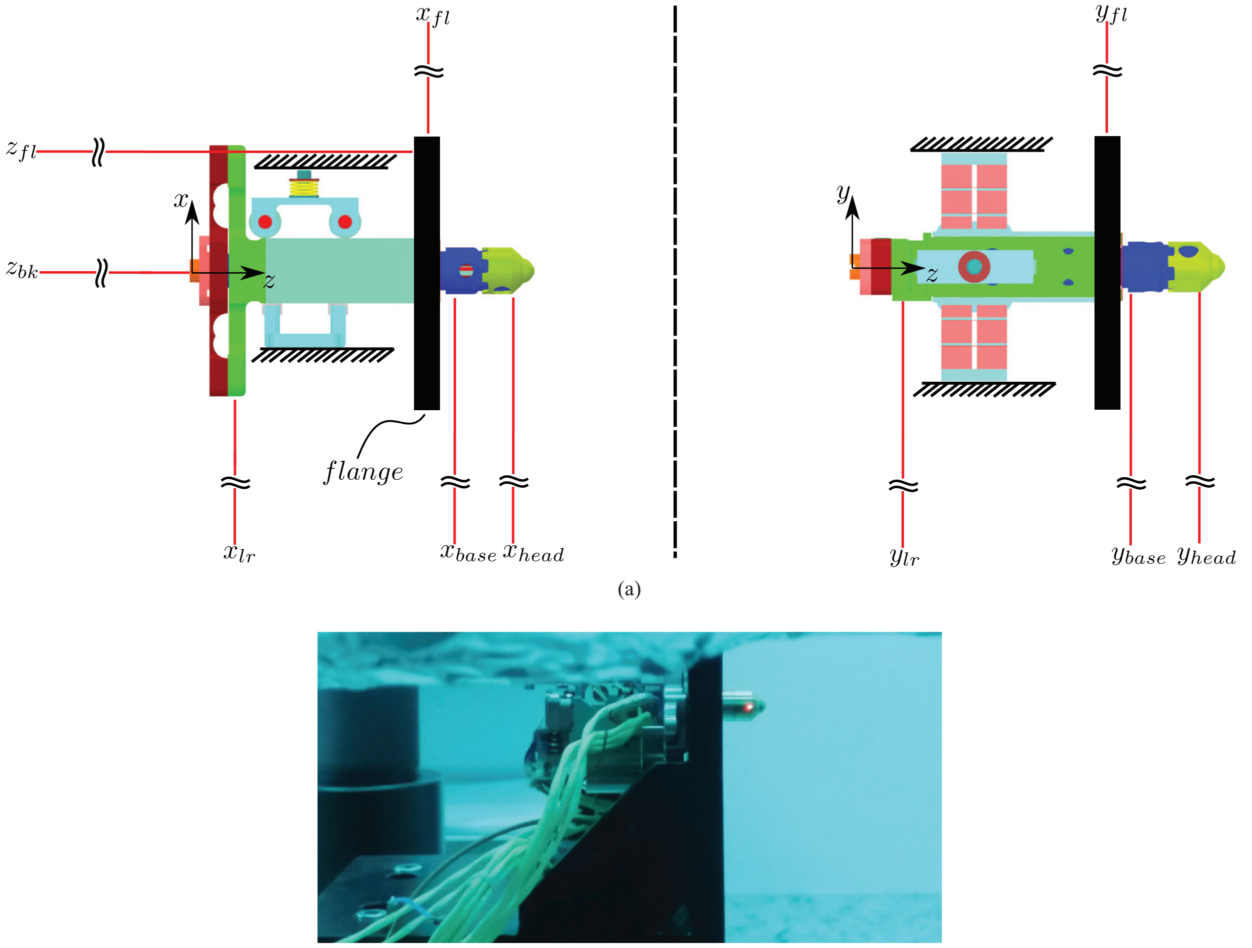

(a)

(b)

Fig. 2. Schematic view of the measurements performed on the x–z plane (top left) and on the y–z plane (top right). On the bottom, picture of the laser pointing the plunger head.

In Section 2 the experimental setup used to characterize the mechanism dynamics is presented. The results are then interpreted in Section 3 to develop the 3D lumped parameter electro-mechanical model of the GPRM. The model physical parameters are estimated through a customized algorithm that simultaneously fits multiple signals, taking into account the shared parameters. The model accuracy is discussed, in the frame of the prediction of its in-flight performance. In Section 4, the model is used to estimate the motion of the predicted impact point with the TM. Based on the model results, the plunger-TM impact hypothesis is investigated and compared with the spacecraft telemetry data. In Section 5, the conclusions drawn from the analysis are presented.

2. The Grabbing Positioning and Release Mechanism ground testing approach

The GPRM mechanism is a release mechanism specifically designed and developed for the LISA Pathfinder mission. The design requirements are very challenging, as the state of the object to be released is restricted to ± 200 μm and ± 2 mrad for translations and rotations, and ± 5 μs^{-1} and ± 100 μrad^{-1} for the linear and angular velocity components respectively (Bortoluzzi et al., 2021c). The mechanism architecture is based on the principle of splitting the grabbing/positioning functions from the release task, together with the mechanical interfaces and related testing strategies (Bortoluzzi et al., 2021c). The plunger is wrapped by a linear runner and a force sensor connects them, providing the measurement of the axial force applied to the TM. The linear runner is moved along the z direction by a piezo walk linear actuator, named nexline. Inside each plunger, a coaxial tip is actuated along the z axis by a voltage-controlled piezo stack actuator. The tip protudes from the plunger head through a dedicated hole: when full voltage is commanded (up to 120 V), the tip is extended toward the TM by approximately 15 μm; conversely when the voltage is shorted, the tip retracts in less than 100 μs. A redundant piezo stack actuator is located in series to the nominal one, separated by a spacer mass. Nominal and redundant piezo may not be operated simultaneously, as they are commanded by two independent electronics units. In Fig. 1b the section view of the mecha-

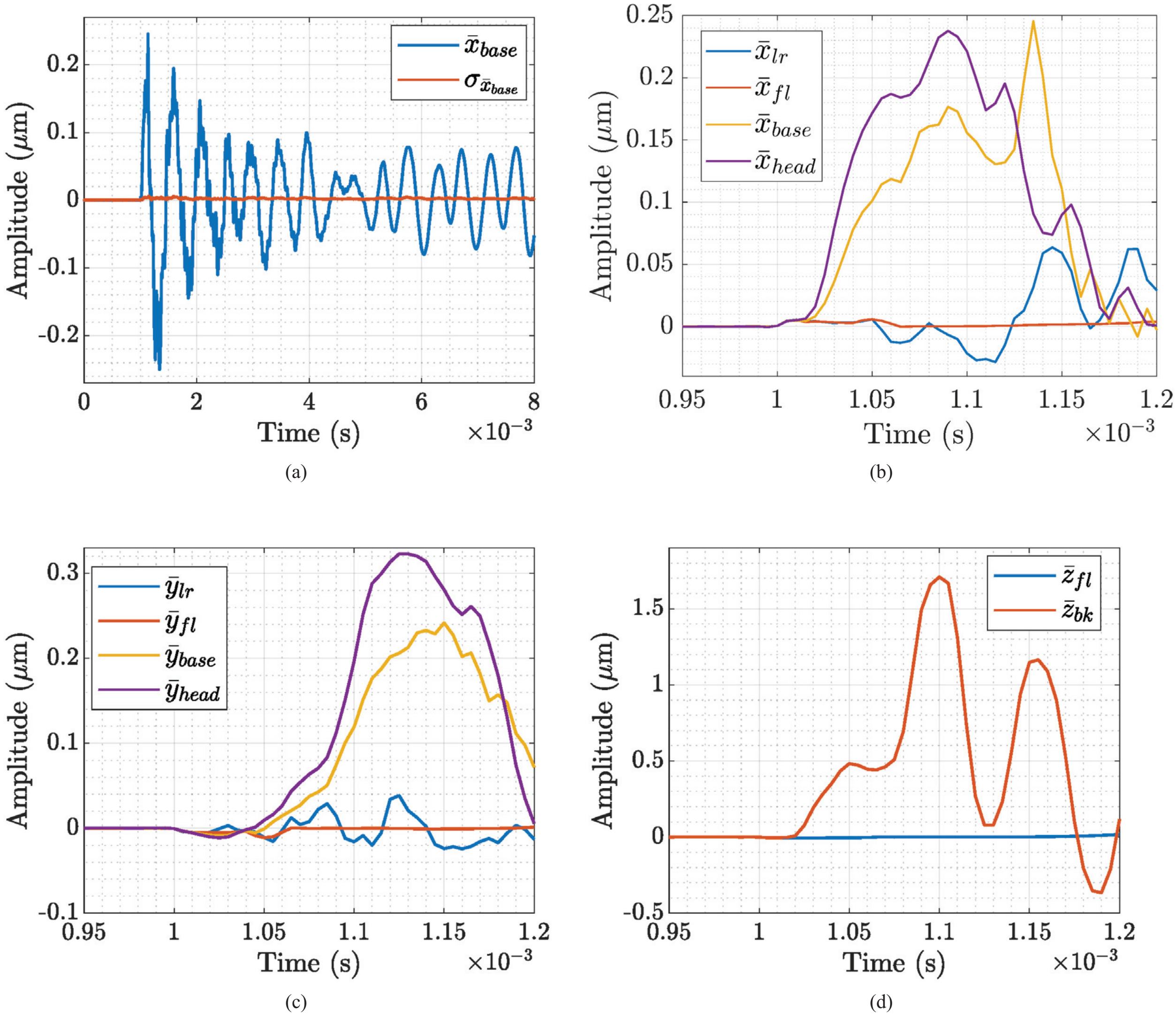

Fig. 3. Plot of the mean signal $\bar{x}_{base}$ together with the standard deviation $\sigma_{\bar{x}_{base}}$ (a) and the synchronized mean signals of the x (b), y (c) and z (d) axes datasets triggered at 1 ms.

nism is depicted, showing the mechanism components located inside the plunger.

The nominal TM release procedure consists of three steps. The first is the grabbing and repositioning of the TM, which is performed by moving the plungers toward the TM until a pre-load force of approximately 1 N is reached and repositioning the grabbed TM in the centre. The second step is the handover: the tips are extended and the plungers simultaneously retracted, maintaining a constant pre-load force (reduced to about 0.3 N). Once the handover is completed, the TM is in pre-release configuration with a nominal distance in the z direction between plunger and TM of 11 μm. The last step is the actual release of the TM, which is performed by simultaneously retracting the tips.

Given the system symmetry, according to the nominal procedure, the TM should acquire velocity only along the z direction at the release. Several experimental campaigns, performed using a dedicated on-ground test facility, demonstrated that the velocity requirements should be fulfilled when the TM is released according to the nominal procedure (references for this testing activity throughout the mechanism conceptualization, design, development and ground testing projects may be found in Bortoluzzi et al., 2020; Bortoluzzi et al., 2008; Bortoluzzi et al., 2009; Bortoluzzi et al., 2010; Benedetti et al., 2011; Bortoluzzi et al., 2013; Bortoluzzi et al., 2015; Zanoni et al., 2015; Bortoluzzi et al., 2016; Bortoluzzi et al., 2017; Bortoluzzi et al., 2013; Zanoni and Bortoluzzi, 2014; Bortoluzzi and Dalla Ricca, 2023; Dalla Ricca et al., 2024.

However, given the unexpected in-flight performance, an additional experimental campaign is carried out at the University of Trento to acquire a set of measurements of the GPRM response at the tip retraction. The experimental setup includes a QM of the GPRM, mounted on an active

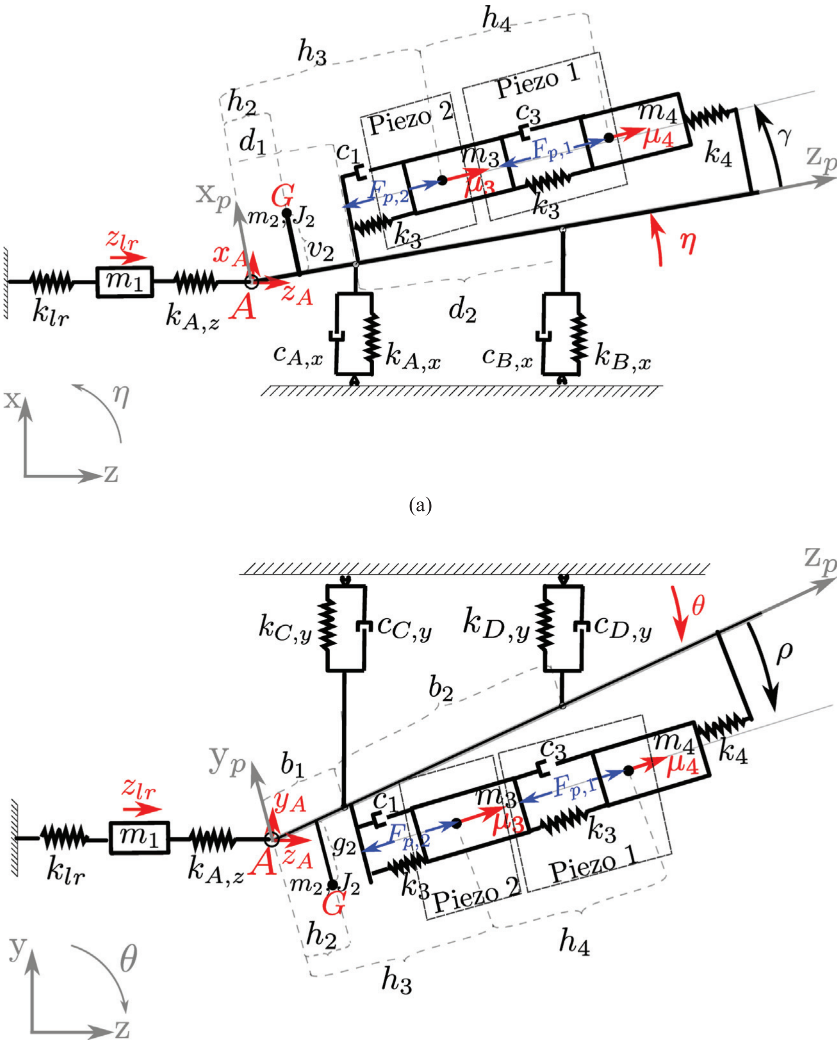

(a)

(b)

Fig. 4. Lumped parameter model of the GPRM on the x–z plane (top) and on the y–z plane (bottom).

Table 1
Ratios between the maximum values reached by the mean signals.

Ratio	Value
$\max(\bar{x}_{head})/\max(\bar{x}_{lr})$	3
$\max(\bar{x}_{head})/\max(\bar{x}_{fl})$	17
$\max(\bar{y}_{head})/\max(\bar{y}_{lr})$	3
$\max(\bar{y}_{head})/\max(\bar{y}_{fl})$	21
$\max(\bar{z}_{bk})/\max(\bar{z}_{fl})$	26

anti-vibration platform. A SIOS laser interferometer is used to characterize the GPRM response, measuring the displacement at 200 kHz. The measurements are repeated by pointing the GPRM in ten different positions, both on the x–z and y–z planes, which are referred to as laser positions in the following. For each laser position a set of ten measurements actuating the system (i.e. retracting the tip) and five noise measurements (tip not actuated) are collected. In Fig. 2a the ten laser positions are schematically depicted (the red lines represent the interferometer laser beam), while in Fig. 2b a picture of the plunger pointed by the laser is shown.

The repeated measurement of the dynamical response of the mechanism in different points yields a large set of signals, which however require adequate post-processing. Three steps are identified:

1. Referring to each laser position, a reference signal is chosen and the remaining nine signals are synchronized with respect to it by minimizing the root mean square of their difference.
2. The mean signal and the standard deviation are computed as a function of time for every data set. As an example, in Fig. 3a, the mean signal of the x_{base} laser position is plotted together with its standard deviation. It can be noted that the vibrations show good repeatability, with a signal to noise ratio approximately equal to 50. The other signals show similar characteristics.

3. The resulting ten mean signals are synchronized such that at a given time (1 ms) the magnitude of their vibration is equal to twice the value of the noise standard deviation ($5 \times 10^{-4}\,\mu$m). This choice guarantees a good compromise between sensitivity and risk of type 1 error in the detection of incipient motion (i.e. wrong rejection of hypothesis of absence of motion). The synchronized mean signals, from now on, are referred to as $\bar{x}_{lr}, \bar{x}_{fl}, \bar{x}_{base}, \bar{x}_{head}, \bar{z}_{bk}, \bar{z}_{fl}, \bar{y}_{fl}, \bar{y}_{lr}, \bar{y}_{base}, \bar{y}_{head}$, where the subscripts $fl, bk, lr, base$ and $head$ stand for flange, plunger back, linear runner, plunger base and plunger head respectively.

As an example, the result of the synchronization procedure is shown in Fig. 3b for the signals acquired pointing the laser in the x direction. A preliminary analysis of the mean signals shows that the plunger vibrations take place mainly along the z axis (axial direction) and the lateral displacements are larger in the neighborhood of its head, where the TM is engaged and released (see Fig. 3b, 3c and 3d).

The mathematical model of the mechanism dynamical response is built focusing on the macroscopic motion of the plunger head, where impacts with the TM may occur. Considering the amplitudes of vibrations (Table 1), the following hypotheses are introduced:

1. the mechanism supporting flange is fixed: $\bar{y}_{fl}, \bar{x}_{fl}$ and $\bar{z}_{fl}$ are neglected,
2. the linear runner does not oscillate along x and y axes: $\bar{y}_{lr}$ and $\bar{x}_{lr}$ are neglected.

Given these considerations, the five signals $\bar{x}_{base}, \bar{x}_{head}, \bar{y}_{base}, \bar{y}_{head}$ and $\bar{z}_{bk}$ are used to fit the model that is described in the next Section.

3. A 3D model of the GPRM dynamics

As stated previously, the analysis presented in Bortoluzzi et al., 2021a is affected by some limitations, mainly:

1. The GPRM models describe only the 2D motion of the mechanism.
2. The two 2D models are not coupled.

These limitations are overcome by developing a fully 3D lumped-parameter electro-mechanical model of the mechanism, which is schematically depicted in Fig. 4 and 5. Modelling a piezo-actuated micro-positioning system is a challenging task, since it may involve the interaction between the actuation side and the mechanism kinematics, including simultaneous non-linear phenomena like creep, vibration and hysteresis Lin et al., 2023. In the present case, the model is developed mainly to describe the retraction dynamics, i.e. to capture the mechanism response to a single quick actuation in the presence of non-idealities like misalignments, eccentricities etc. As a consequence, different level of details are adopted to describe the mechanical and electrical subsystems. The model kinematics is approached using the small angle approximation and considering that the rotation of the plunger about its geometrical axis is neglected, as there is no evidence of its contribution to the TM state after the in-flight release (Bortoluzzi et al., 2021c). The mechanism is modeled by four rigid bodies:

1. the linear runner is described as a body with mass m_1 centered in point A. The body is allowed to slide only along the z direction and it is connected to the ground and to the plunger through springs k_{lr} and $k_{A,z}$ respectively.
2. The plunger is described as an axial-symmetric body with mass m_2 and moment of inertia J_2. A reference frame is fixed to the plunger with the z_p axis aligned with its geometrical axis and axes x_p and y_p defined as shown in Fig. 4. The eccentricity of the plunger center of mass (CoM) is described by the parameters v_2, g_2 and h_2, while the plunger attitude is described by a rotation η about the y_p axis and θ about the x_p axis. The plunger is connected to the ground along the x direction through

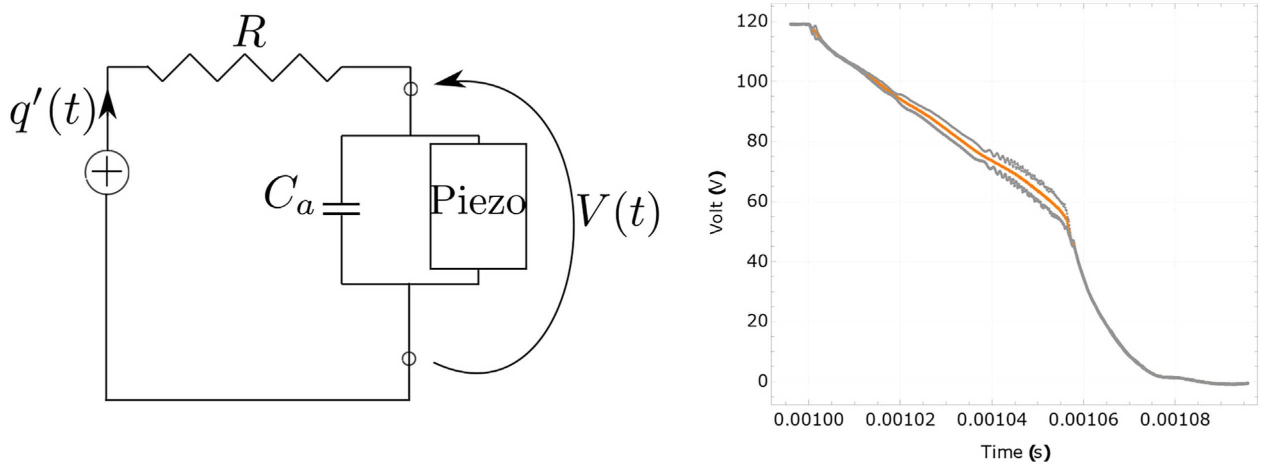

Fig. 5. On the left, functional scheme of the electrical circuit commanding the piezo actuator (Bortoluzzi et al., 2021b; Adriaens et al., 2000). On the right, mean commanding voltage signal $V(t)$ of the tip retraction along with its standard deviatio.n (gray curves).

Table 2
Fitting and constant parameters.

Parameter	Unit	Description
v_2	mm	plunger CoM x coordinate in the plunger body-fixed reference frame
g_2	mm	plunger CoM y coordinate in the plunger body-fixed reference frame
γ	rad	spacer and tip misalignment with respect to the plunger geometrical axis on the x–z plane
ρ	rad	spacer tip misalignment with respect to the plunger geometrical axis on the y–z plane
k_{lr}	kg s^{-2}	spring connecting the plunger to the ground
$k_{A,x}$	kg s^{-2}	spring connecting the plunger to the ground
$k_{B,x}$	kg s^{-2}	spring connecting the plunger to the ground
$c_{A,x}$	kg s^{-1}	damper connecting the plunger to the ground
$c_{B,x}$	kg s^{-1}	damper connecting the plunger to the ground
$k_{C,y}$	kg s^{-2}	spring connecting the plunger to the ground
$k_{D,y}$	kg s^{-2}	spring connecting the plunger to the ground
$c_{C,y}$	kg s^{-1}	damper connecting the plunger to the ground
$c_{D,y}$	kg s^{-1}	damper connecting the plunger to the ground
m_1	g	linear runner mass
m_2	g	plunger mass
m_3	g	spacer mass
m_4	g	tip mass
d_1	mm	distance of $k_{A,x}$ and $c_{A,x}$ from A
d_2	mm	distance of $k_{B,x}$ and $c_{B,x}$ from $k_{A,x}$ and $c_{A,x}$
b_1	mm	distance of $k_{C,y}$ and $c_{C,y}$ from A
b_2	mm	distance of $k_{D,x}$ and $c_{D,x}$ from $k_{C,x}$ and $c_{C,x}$
t_0	s	time lag of the dynamic response with respect to the commanding signal
t_1	s	time lag to propagate the vibrations from the tip to the plunger back
h_3	0.0421 m	distance of the spacer from A
h_4	0.0192 m	distance of the tip from the spacer
J_2	2.7×10^{-6} kg m^{-2}	plunger inertia
$k_{A,z}$	2.1×10^{6} kg s^{-2}	spring connecting the plunger to the linear runner
k_3	2.0×10^{7} kg s^{-2}	damper connecting the tip to the spacer and the spacer to the plunger
k_4	9.8×10^{4} kg s^{-2}	spring connecting the tip to the plunger
c_1	1.3kg s^{-1}	damper connecting the spacer to the plunger
c_3	1.4 kg s^{-1}	damper connecting the tip to the spacer
T_{em}	2.6 C m^{-1}	piezo effect
C_a	5.0×10^{-7}F	capacitance of the electrical circuit commanding the piezo
R	19.06Ω	resistance of the electrical circuit commanding the piezo

springs and dampers $k_{A,x}, k_{B,x}, c_{A,x}$ and $c_{B,x}$. The positions of $k_{A,x}$ and $c_{A,x}$ and of $k_{B,x}$ and $c_{B,x}$ with respect to the plunger back are identified by the parameters d_1 and $d_1 + d_2$ respectively. Similarly, on the y direction, the plunger is connected to the ground through springs and dampers $k_{C,y}, k_{D,y}, c_{C,y}$, and $c_{D,y}$. Their positions with respect to the plunger back are identified by the parameter b_1 and $b_1 + b_2$ respectively.

3. The spacer and the tip are described as bodies with mass m_3 and m_4 respectively. They are connected to each other through springs and dampers c_3 and k_3 and to the plunger through springs and dampers c_1, k_3 and k_4. When no voltage is supplied to the piezo-stack, the CoMs of the two bodies lie along the longitudinal axis of the plunger. When full voltage is applied, the bodies move along the axis determined by the unknown angles γ and ρ.

The eccentricity of the plunger and CoM and the misalignment of spacer and tip are assumed to be constant and inevitable during the assembly and integration process due to factors such as alignment errors and machining tolerances. The piezo actuators are modelled as massless electro-mechanical devices which are characterised by a mechanical interface (force, displacement) and an electrical interface (voltage and current) as shown in Fig. 5. As shown in Fig. 4, the mechanical DoFs are highlighted in red while the blue arrows represent the force applied by the piezo actuators.

A linear model is adopted to describe the piezo electro-mechanical dynamics in terms of input–output relationship (Yue et al., 2010). The relationship derived in the following and expressed in Eq. 1 provides the exerted force $F_{p,i}$ by the piezo as a function of the cumulated charge $q(t)$ (Bortoluzzi et al., 2011 and Standard, 1988), with $i \in \{1, 2\}$. In particular, the pedix 1 refers to the nominal piezo stack actuator, located between spacer and tip, while the pedix 2 refers to the redundant piezo actuator, located between plunger and spacer.

$$\begin{cases} F_{p,1} & = \frac{T_{em} q(t)}{C_a} - \frac{T_{em}^2 (\mu_4(t) - \mu_3(t))}{C_a} \\ F_{p,2} & = \frac{T_{em} q(t)}{C_a} - \frac{T_{em}^2 (\mu_3(t))}{C_a} \end{cases} \quad (1)$$

where T_{em} is the constant representing the piezo-effect and C_a the capacitance of the piezo.

The equation describing the evolution of the electrical charge $q(t)$ is derived using Kirchoff laws (Fig. 5) and considering that the input voltage $V(t)$ is shifted in time by adding the parameter t_0, which describes the time lag of the dynamic response with respect to the commanding signal.

The input to the model is the voltage commanding the piezo-stack actuator and the related output is the tip retraction. In order to characterize it, ten tip retraction tests are performed measuring the voltage time history with a digital DSO7032A Agilent Technologies oscilloscope. The mean voltage signal $V(t)$ is computed and plotted in Fig. 5: the retraction command is sent at approximately 1 ms (i.e. the voltage starts to decrease).

The outputs of the model are the axial motion of the linear runner ($z_{lr}(t)$) and of the plunger back ($z_A(t)$), the motion of the plunger back along x and y ($x_A(t)$ and $y_A(t)$ respectively), the plunger attitude about the y and x axes ($\eta(t)$ and $\theta(t)$ respectively), the spacer and tip displacements with respect to the plunger ($\mu_3(t)$ and $\mu_4(t)$ respectively) and the electrical charge $q(t)$ flowing in the circuit commanding the piezo actuator (see Fig. 5). The equations describing the mechanism dynamics are derived following the Lagrange approach and are completed by the constitutive equation of the piezo-stack actuator. The set of equations may be written in matrix form as:

$$M(\alpha,\beta)\,\xi''(t) + C(\alpha,\beta)\,\xi'(t) + K(\alpha,\beta)\,\xi(t) - u(t) = 0 \tag{2}$$

where M, C and K represent the 9×9 mass, damping and stiffness matrices respectively; α and β are the vectors containing the fitting and constant parameters respectively (summarized in Table 2); $\xi(t)$ the vector collecting the DoF of the model and $u(t)$ the 9×1 input vector. For the sake of completeness, the detailed complete set of equations is reported in A.

3.1. Parameter estimation algorithm

The fitting parameters have to be estimated through a fitting procedure starting from their nominal values (which can be deducted either from the results of the fitting procedure described in Bortoluzzi et al., 2021a or from the CAD model of the mechanism); the values of the constants are estimated from either the results of the analysis presented in Bortoluzzi et al., 2021b or the GPRM documentation.

According to the dynamical model, the measured signals can be predicted as functions of the system outputs (Eqn. 3), after the integration of the equations of motion through the Implicit Differential–Algebraic (IDA) method (Wolfram, 2003). The Equations are derived assuming small rotations and the presence of a time lag t_1 (on the order of μs) between the motion of the plunger back with respect to the plunger head, where the actuator is located. The starting guess of t_1 is estimated considering the ratio between the length of the mechanism and the velocity of a longitudinal wave propagating along the mechanism.

$$\begin{aligned}
z_{bk}(t,\alpha,\beta) &= z_A(t-t_1)\\
x_{base}(t,\alpha,\beta) &= x_A(t) + \eta(t)d_{x,base}\\
x_{head}(t,\alpha,\beta) &= x_A(t) + \eta(t)d_{x,head}\\
y_{base}(t,\alpha,\beta) &= y_A(t) + \theta(t)d_{y,base}\\
y_{head}(t,\alpha,\beta) &= y_A(t) + \theta(t)d_{y,head}
\end{aligned} \tag{3}$$

where α is the vector containing the fitting parameters, β the vector containing the constant parameters and $d_{x,base}, d_{x,head}, d_{y,base}, d_{y,head}$ represent the distance of the laser positions $x_{base}, x_{head}, y_{base}, y_{head}$ from the plunger back (which are estimated from the CAD model of the mechanism).

When a model is available to describe the response of a dynamical system, it is often formulated in a parametric form such that, by minimizing the deviation of the predicted response from the measured data, an estimation of the parameters can be produced. It is demonstrated in Bard, 1974 that the information associated to such a deviation is minimized by the multivariate normal distribution, which is assumed as the reference distribution. Once the parametric model of the system is formulated, the likelihood function expresses the joint probability density function of the observations q^* as a function of the model parameters vector $\alpha \in \mathbb{R}^p$, where p is the number of fitting parameters (Šimænek and Hopmans, 2020):

$$L(\alpha) = (2\pi)^{-\frac{n}{2}} \det(V)^{-\frac{1}{2}} \mathrm{e}^{-\frac{1}{2}[q^*-\hat{q}(\alpha)]^T V^{-1}[q^*-\hat{q}(\alpha)]} \tag{4}$$

where V is the covariance matrix of the measurement errors, n is the total number of observations and $\hat{q}$ is the model prediction. The difference between the measured and estimated quantities (i.e. $q^*-\hat{q}(\alpha)$) is called residual.

The following problem is formulated considering that the vector of observations q^* is composed of s different signals (appended in sequence $r = 1,\ldots,s$; with $s = 5$), assuming that the response of the dynamical system is measured in some points (namely the mechanism base, head and back) and along some directions (namely x, y and z), collecting n samples for each signal and N total samples ($N = s\times n$). For simplicity, it is also assumed that the measurement errors are uncorrelated and characterised by a time dependent variance. Therefore, the covariance matrix V is diagonal, collecting in sequence the variance of the disturbance superimposed to every signal at each time stamp (Draper and Smith, 1998; Wagner and Gorelick, 1986). No prior information is assumed for the parameters vector α. The logarithm of the likelihood function can be calculated as follows:

$$\ln(L(\alpha)) = \sum_{r=1}^{s}\left(-\frac{N}{2}\ln 2 - \sum_{w=1}^{n}\ln\sigma_{w+(r-1)n} - \frac{1}{2}\sum_{w=1}^{n}\frac{\left(q^*_{w+(r-1)n} - \hat{q}_r(\alpha,t_w)\right)^2}{\sigma^2_{w+(r-1)n}}\right) \tag{5}$$

where, for signal r, $q^*_{w+(r-1)n}$ is the w-th observation, $\hat{q}_r(\alpha,t_w)$ is the estimated response of the system at the w-th instant and $\sigma^2_{w+(r-1)n}$ is the variance of the w-th sample.

The vector that maximizes L is the same vector that minimizes the last term in Eqn. 5, namely the weighted least square function. Under the hypothesis of disturbances described by a multivariate normal distribution with time dependent variance, it is possible to state that the weighted least square function behaves as a Chi-squared distribution with $N-p$ degrees of freedom. Therefore, for the present case of study, it is possible to write that:

$$\chi^2(\alpha) = \sum_j \left(\sum_{w=1}^{n} \left(\frac{\bar{x}_j(t_w) - x_j(\alpha, t_w)}{\sigma_j(t_w)} \right)^2 \right) + \sum_j \left(\sum_{w=1}^{n} \left(\frac{\bar{y}_j(t_w) - y_j(\alpha, t_w)}{\sigma_j(t_w)} \right)^2 \right) + \sum_{w=1}^{n} \left(\frac{\bar{z}_{bk}(t_w) - z_{bk}(\alpha, t_w)}{\sigma_{bk}(t_w)} \right)^2 \tag{6}$$

where $j \in \{base, head\}$, t_w corresponds to the w-th sampling time instant, n is the total number of sampling points of each mean signal and $\sigma_j(t_w)$ is the signal standard deviation at the w-th time instant.

The $\chi^2(\alpha)$ function is highly non linear in the parameters, therefore the optimization has to be performed iteratively in order to increase the probability of finding the global minimum. Given the non-linearity of the problem formulation, the Levenberg–Marquardt algorithm (LMA) is adopted to minimize the $\chi^2(\alpha)$ function. The LMA results from the blend of the gradient descent and Gauss–Newton iteration methods. The former optimizes the parameters values in the direction opposite to the gradient of the least square function, converging well for problems with simple objective function (Madsen et al., 2004). The latter minimizes a sum of squares objective function under the assumption that the least square function is quadratic in the parameters values near the optimal solution, typically converging faster than the gradient descent method (Marquardt, 1963). The LMA changes the parameters update $\Delta\alpha$ through the damping factor λ between the two methods. The update relationship is defined in Algorithm 1. Small values of λ result in a Gauss–Newton update, while large λ values result in a gradient descent update. The damping factor is initialized to be large so that first updates are in the descent direction. If an iteration results in a worse value of $\chi^2(\alpha)$, then λ is increased; otherwise λ is decreased and the algorithm approaches the Gauss–Newton method (Gavin, 2019). The algorithm is stopped when $\chi^2(\alpha)$ falls below a certain threshold, the difference between two consecutive values of $\chi^2(\alpha)$ is small enough or the maximum number of iterations is reached.

Algorithm 1. Levenberg–Marquardt algorithm

```
Given initial values $\alpha^0$ and $\lambda^0$
for $i = 0 \ldots m$ do
    for $r = 1 \ldots s$ do        ▷Build Jacobian $J^{r,i}$
        for $k = 1 \ldots p$ do
            for $w = 1 \ldots n$ do
                $J^{r,i}_{w,k} = \frac{\partial \hat{q}_r(\alpha, t_w)}{\partial \alpha_k}\Big|_{\alpha=\alpha^i}$
            end for
        end for
    end for
    $J^i = \mathrm{Join}(J^{r,i}), \quad r \in \{1, \ldots, s\}$        ▷Stack
    vertically the Jacobians
    $J^i_x = D\,J^i$
    $\left[ (J^i_x)^T\ (J^i_x) + \lambda_i\ \mathrm{diag}\left( (J^i_x)^T\ (J^i_x) \right) \right]$
    $\Delta\alpha = -(J^i_x)^T\ D\,e^i$        ▷Find update $\Delta\alpha$
    $\alpha^{i+1} = \alpha^i + \Delta\alpha$        ▷Update parameters
    if $\chi^2(\alpha^{i+1}) \geqslant \chi^2(\alpha^i)$ then
        $\lambda^{i+1} = 10\lambda^i$
    else
        $\lambda^{i+1} = \lambda^i/10$
    end if
    if $|\chi^2(\alpha^{i+1}) - \chi^2(\alpha^i)| \leqslant \varepsilon_1$ or $\chi^2(\alpha^{i+1}) \leqslant \varepsilon_2$ then
        break
    end if
end for
```

In Algorithm 1, i is the current iteration, m is the maximum number of iterations (user-defined), $e^i \in \mathbb{R}^{sn}$ is the vector of the fit residuals, $J^i \in \mathbb{R}^{sn \times p}$ is the Jacobian matrix of the five numerical functions, D is the Cholesky decomposition of the weighting matrix $W := V^{-1} \in \mathbb{R}^{sn \times sn}$ and $\varepsilon_1, \varepsilon_2$ are user-defined tolerances.

Since the risk of impact between plunger head and TM is maximum when the vibrations are larger, according to Fig.s 3b, 3c and 3d, the time interval of interest is limited to [0.97 ms, 1.2 ms], where the displacement overshoot is produced. The assumption is supported by the analyses reported inBortoluzzi et al., 2021b. The minimization algorithm is highly sensitive to the initial values of the parameters. Therefore, the minimization algorithm is repeated 1000 times varying randomly the initial guess of the param-

Table 3
Best fit parameters.

Parameter	Value	Nominal value	Initial value
v_2	(2.7 ± 0.2) mm	/	2.8 mm
g_2	(-0.4 ± 0.1) mm	/	–0.4 mm
γ	(-7 ± 2) mrad	/	5 mrad
ρ	(37 ± 3) mrad	/	37 mrad
k_{lr}	$(164 \pm 1)\times 10^4$ kg s^{-2}	/	166×10^4 kg s^{-2}
$k_{A,x}$	$(1104 \pm 7) \times 10^5$ kg s^{-2}	/	1123×10^5 kg s^{-2}
$k_{B,x}$	$(223 \pm 2) \times 10^3$ kg s^{-2}	/	232×10^3 kg s^{-2}
$c_{A,x}$	(1.07 ± 0.01) kg s^{-1}	/	0.099 kg s^{-1}
$c_{B,x}$	(21.6 ± 0.7) kg s^{-1}	/	23 kg s^{-1}
$k_{C,y}$	$(7 \pm 1) \times 10^6$ kg s^{-2}	/	6×10^6 kg s^{-2}
$k_{D,y}$	$(50 \pm 6) \times 10^5$ kg s^{-2}	/	54×10^5 kg s^{-2}
$c_{C,y}$	(1.50 ± 0.02) kg s^{-1}	/	1.57 kg s^{-1}
$c_{D,y}$	(1.61 ± 0.01) kg s^{-1}	/	1.72 kg s^{-1}
m_1	(0.4 ± 0.1) g	/	0.4 g
m_2	(12.4 ± 0.9) g	12.3 g	12.7 g
m_3	(1.7 ± 0.3) g	1.5 g	1.9 g
m_4	(0.5 ± 0.3) g	0.39 g	0.3 g
d_1	(2 ± 2) mm	/	2 mm
d_2	(40 ± 3) mm	/	45 mm
b_1	(42 ± 4) mm	/	39 mm
b_2	(4 ± 6) mm	/	4 mm
t_0	$(4 \pm 3) \times 10^{-6}$ s	/	5×10^{-6} s
t_1	$(5 \pm 3) \times 10^{-6}$ s	/	4×10^{-6} s

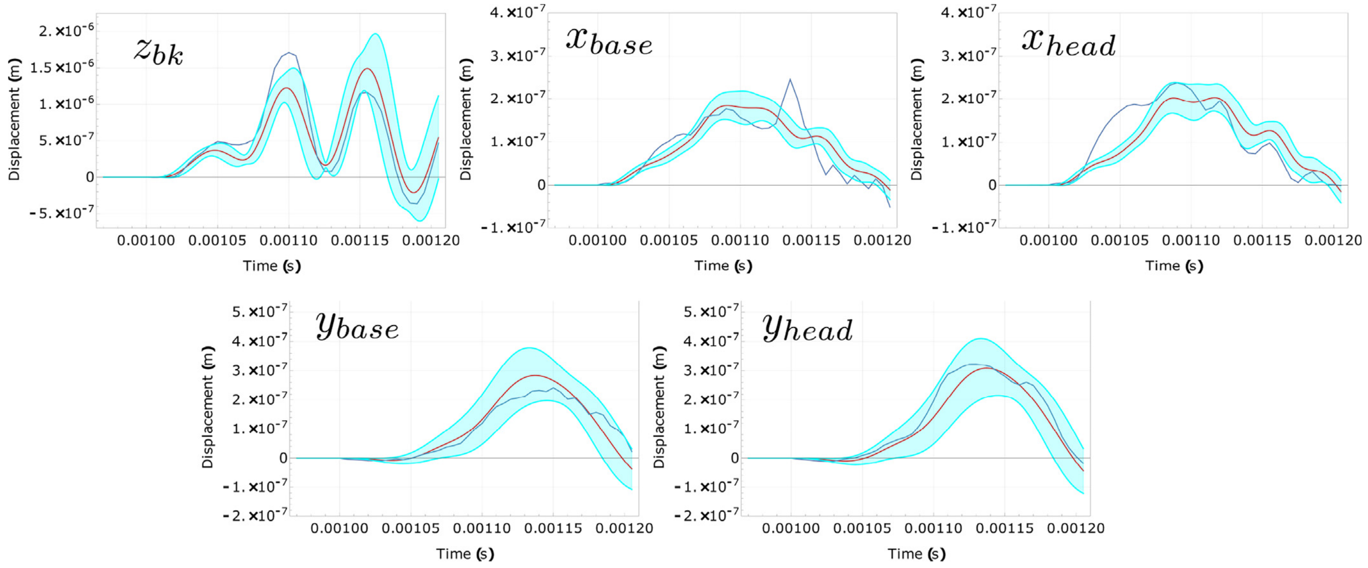

Fig. 6. Magnified plots of the best fit result.

eters in the range ±20% of their nominal values. The fitting iteration that returned the smallest value of χ^2 is referred to as best fit; the corresponding set of parameters (which are reported in Table 3 along with their uncertainties), Jacobian and residuals are denoted as α^*, J_x^* and e^* respectively. The best fit is plotted in Fig. 6. The blue curves represent the mean signals, the red curves represent the best fit provided by Eqn. 3 and the cyan curves are obtained propagating the model parameter uncertainties. Despite advanced method to compute the uncertainty are present in the literature, in this case the parameters uncertainties can be estimated under the assumption that the solution converges to a global minimum, so that the parameters' uncertainties are limited to measurement errors only (Šimænek and Hopmans, 2020). The parameters covariance matrix $C \in \mathbb{R}^{p\times p}$ is estimated considering Eqn. 7 (Kool and Parker, 1988).

$$\begin{aligned} C &= \frac{(e_x^*)^T e_x^*}{(sn-p)} \left((J_x^*)^T J_x^*\right)^{-1} \\ e_x^* &= D\, e^* \end{aligned} \tag{7}$$

The results plotted in Fig. 6 and reported in Table 3 show that both angular misalignment and rotational dynamic response are on the order of mrad, which comply with the hypothesis of small angles and model lnearisation.

Due to the simplifying hypothesis introduced in the development of the model, some deviations are present between the predicted and measured dynamic response, as shown in Fig. 6. A quality assessment of the fit is proposed based on two considerations, showing that the limitations in the fitting results do not significantly hinder the model-based prediction of the in-flight dynamics.

The first consideration is carried out by comparing the plunger mass value estimated by the fitting procedures for the 2D (Bortoluzzi et al., 2021b) and 3D model cases with its nominal value. As illustrated in Fig. 7, the mass value computed for the 3D model (orange point) is closer to its nominal value (green point, which is derived from the CAD model of the mechanism) and its uncertainty is smaller than those for the two 2D cases (red points). Similar results hold also for the mass values of linear runner, spacer and tip.

The second consideration is based on an energetic approach (Akhan et al., 2023). It is demonstrated in Bortoluzzi et al., 2021c; Bortoluzzi et al., 2021b that the in-flight impacts at the release are compatible with the hypothesis of energy conservation. As a consequence, the quality of the model is evaluated by comparing the histograms of the measured and simulated kinetic energies, according to the procedure described in Bortoluzzi et al., 2021b. Referring to Fig. 8, the yellow rectangles describe the kinetic energy predicted by the 3D model, while the blue rectangles refer to the measured kinetic energy. The x axis of the plot represents energy bins, while the y axis represents the time during which the kinetic energy assumes values in the bins. The orange error bars are obtained propagating the model parameter uncertainties on the predicted kinetic energy, while the blue ones are obtained propagating the uncertainties on the measured kinetic energy. Even if the analytical model predicts a slightly higher maximum kinetic energy, the plot shows that the measured kinetic energy lies almost totally inside the uncertainty bars of the predicted kinetic energy. The model is therefore assumed representative of the mechanism energy-conservative impact dynamics.

4. Prediction of the in-flight plunger-TM dynamics at the tip retraction

The prediction of the TM impact dynamics relies on the knowledge of the motion of its CoM and of the impact point. Defined x_G, y_G, and z_G the projections of the plunger CoM positions along the x, y and z direction respectively,

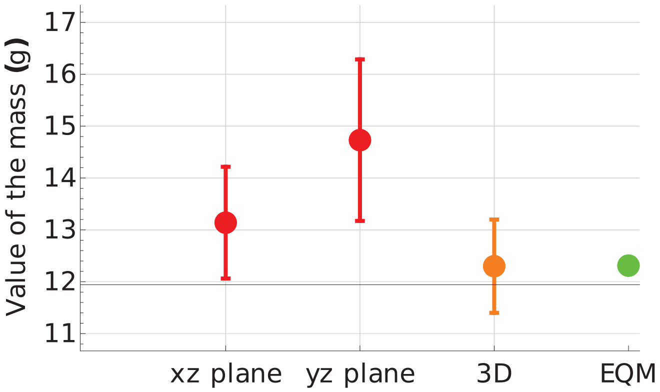

Fig. 7. Plunger mass values estimated by the fitting procedures for the 2D (red points) and 3D (orange point) model cases together with its nominal value (green point). In the x axes, *xz* and *yz* planes refer to the masses values obtained in Bortoluzzi et al., 2021a, 3D to the value reported in Table 3 and EQM to the values obtained from the CAD model of th.e LPF mechanism.

the plunger CoM trajectory can be estimated considering Eqn. 8.

$$
\begin{aligned}
&x_G(\alpha^*,t) = v_2cos(\eta(\alpha^*,t)) + h_2sin(\eta(\alpha^*,t)) + x_A(\alpha^*,t)\\
&y_G(\alpha^*,t) = g_2cos(\theta(\alpha^*,t)) - h_2cos(\eta(\alpha^*,t))sin(\theta(\alpha^*,t))\\
&\quad +v_2sin(\eta(\alpha^*,t))sin(\theta(\alpha^*,t)) + y_A(\alpha^*,t)\\
&z_G(\alpha^*,t) = h_2cos(\theta(\alpha^*,t))cos(\eta(\alpha^*,t))\\
&\quad -v_2cos(\theta(\alpha^*,\alpha^*,t))sin(\eta(\alpha^*,\alpha^*,t)) + g_2sin(\theta(\alpha^*,t))\\
&\quad +z_A(\alpha^*,t) + z_{lr}(\alpha^*,t)
\end{aligned}
\tag{8}
$$

A similar analysis can be carried out considering the motion of the expected impact point. Even if its position is not known a priori, the particular geometries of the plunger head and of the TM indents suggest that the impact point belongs to the nominal areas of plunger head-TM contact, represented by the blue and red lines depicted in Fig. 9. When the plunger is still, the blue line is located on the x–z plane, while the red line is located on the y–z plane. The middle points of every line are defined as M_{xz} and M_{yz}, whose components are $(dist_x,0,dist_z)$ and $(0,dist_y,dist_z)$ in the reference frame centered on the plunger CoM.

In Fig. 10 the trajectories of M_{xz}, M_{yz} and the tip activating Piezo 2 are depicted, projected on the x–z, y–z and x–y planes. The blue and red asterisks represent their positions at the initial time instant and at the final time instant (i.e. *t* equal to 1.2 ms) respectively. It can be noticed that the axial dynamics, which is dominant, is coupled to both lateral axes, with non negligible overshoot and possible impact implications. When the trajectory of the plunger intersects the TM indent surface, an impact occurs. This condition depends on the actual plunger-TM relative configuration at the release, which directly affects the available gaps and, in turn, the risk of collision. Since the relative configuration is affected by some uncertainty, the approach here followed aims at finding a compatibility scenario between the TM state detected at the in-flight release and the state predicted by an impact model applied to the plunger-TM pair.

The dynamics of impact and the mitigation of the related effects, even if restricted to the mechanism framework, is quite a wide research topic. In the literature, impacts are usually categorized in two ways (Khandelwal and Mukherjee, 2024): continuous and instantaneous models (Brach, 1989). The case of study here dealt with is focused on the full prediction of the post-impact state of the body impacted by the mechanism, therefore a 6 degrees

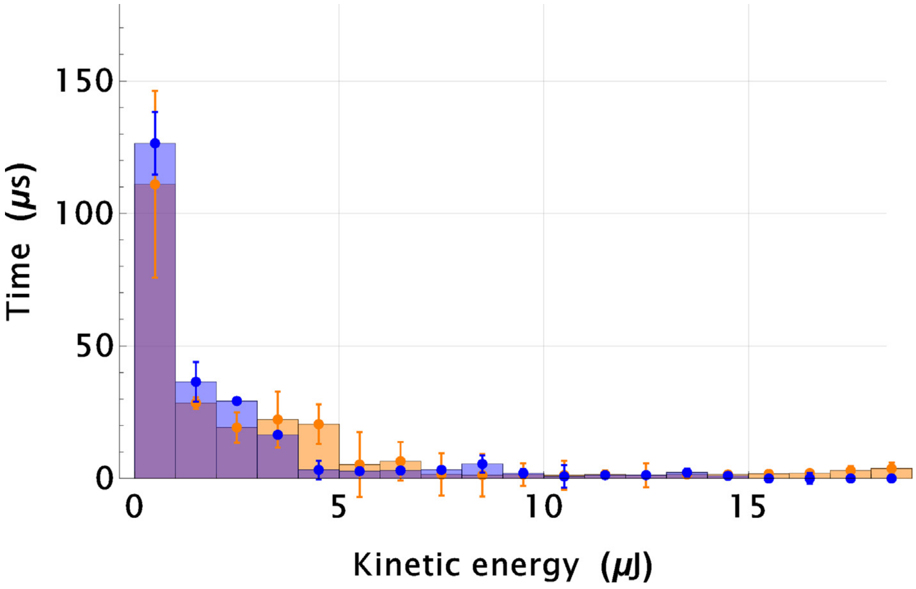

Fig. 8. Kinetic energy histogram: yellow rectangles represent the kinetic energy predicted by the 3D model, while the blue rectangles refer to the measured kinetic energy.

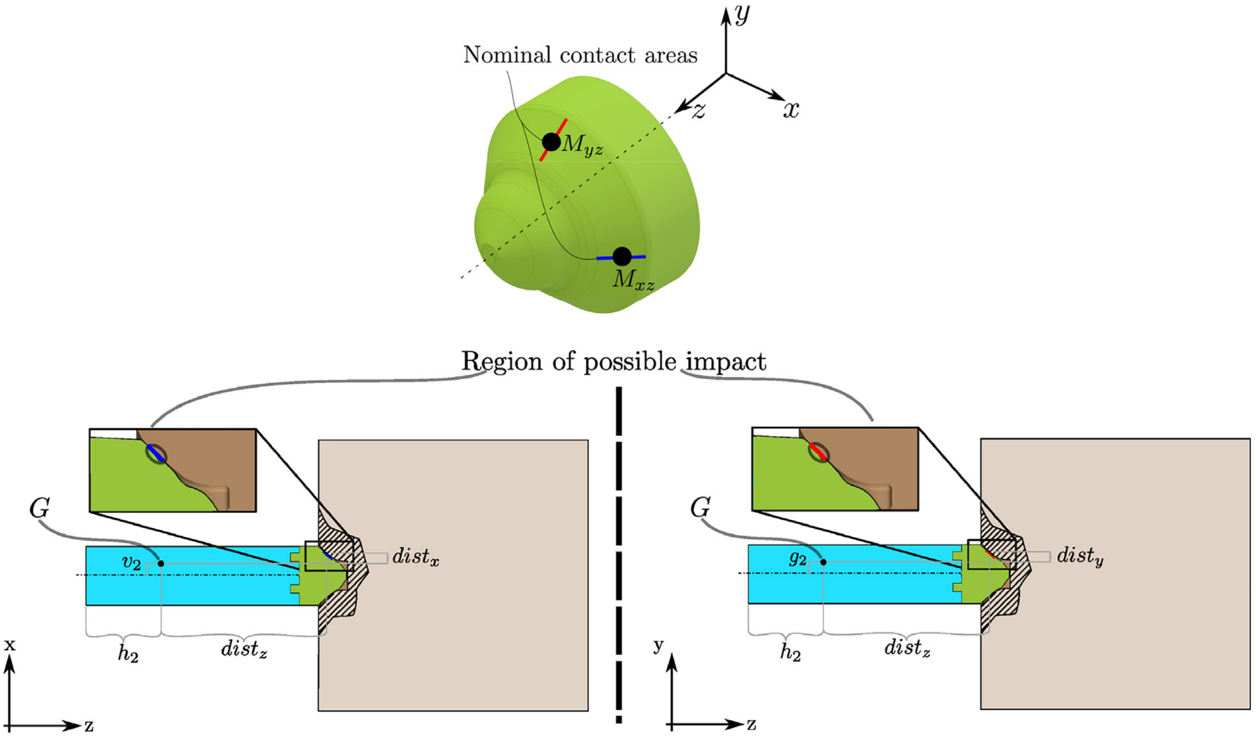

Fig. 9. Rendering of the plunger head (top) and schematic section views of the contact areas (bottom).

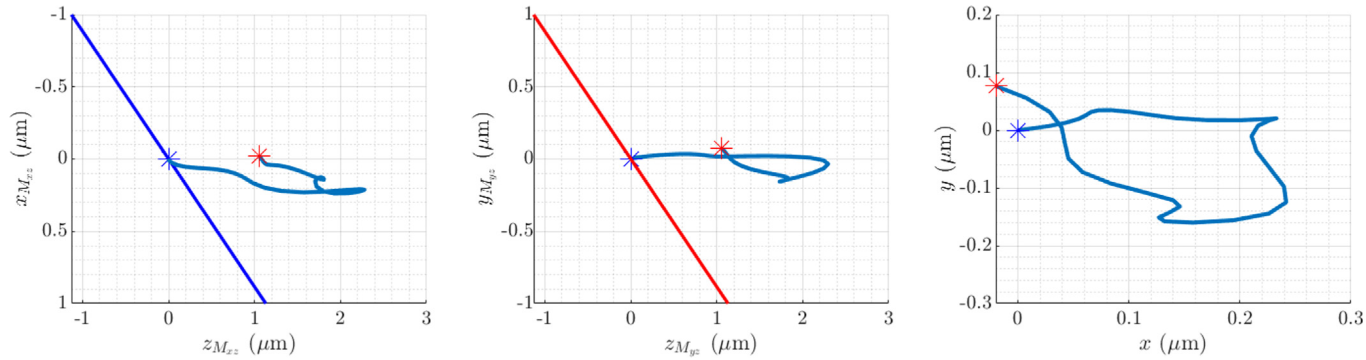

Fig. 10. Trajectory of M_{xz} projected on the x–z plane (left) and of M_{yz} on the y–z plane (middle). Trajectory of the tip edge projected on the x–y plane (right).

of freedom observable must be addressed. For this reason, according to Bortoluzzi et al., 2021b and Zabuga, 2016 simple hypotheses on the impact dynamics are introduced and applied to the two planes of the post-release TM motion (x–z and y–z in Fig. 9):

1. The strains produced by the impact on the two bodies are small if compared to their dimensions.
2. The impact forces are dominant if compared to the other forces acting in the mechanical system.
3. The collision is perfectly elastic, instantaneous and occurs only one time.
4. The impulse received by the TM is orthogonal to the impacting surface.

The equations are solved for each plane (the solution just for the x–z plane is reported in B) in order to have the post-impact TM state (x, z, η and y, z, θ velocities) as a function of the time of impact, i.e. the TM state is calculated as if the impact occurred at the generic timestamp t. The model compatibility with the in-flight results is then verified by comparing the actual TM state with the prediction.

4.1. Impact model validation with in-flight data

An example of an in-flight test telemetry signal is reported in Fig. 11a, where the blue dots correspond to the x-component of the released TM displacement. The

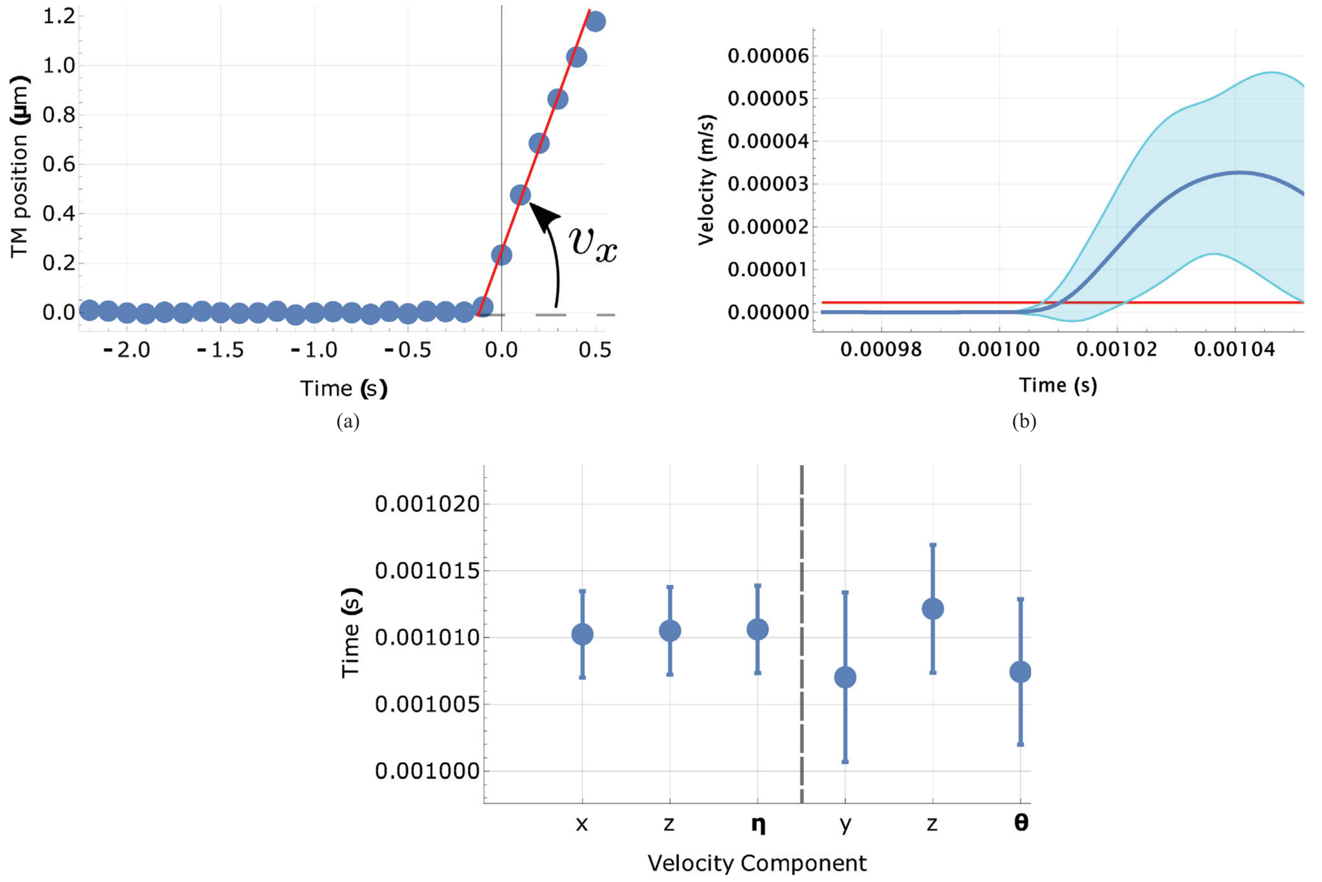

(a)

(b)

(c)

Fig. 11. Example of impact analysis of an in-flight test.

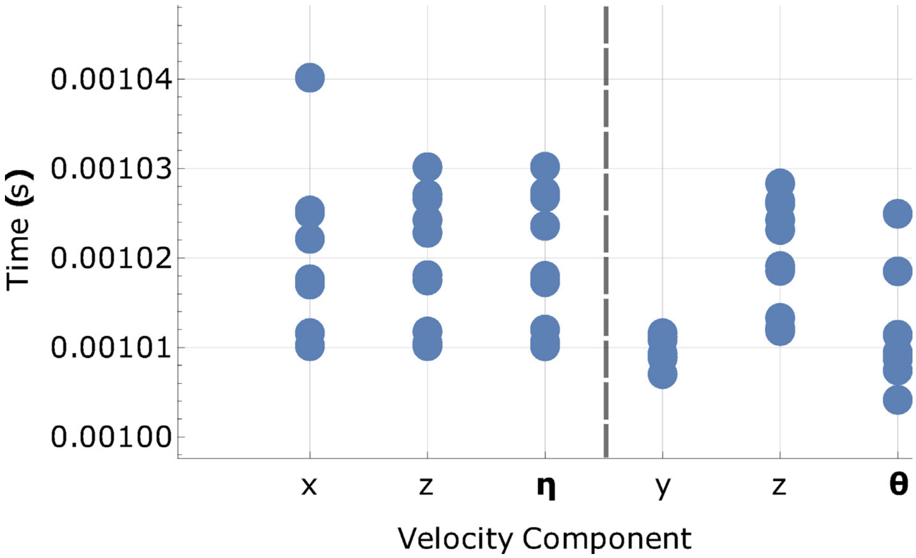

Fig. 12. All 66 estimated impact time instants.

in-flight release happens at time $t_0 = 0$ and the slope of the line interpolating the points after t_0 gives the x-component of the released TM velocity, which is the red line in Fig. 11b. The blue curve in Fig. 11b represents the x-component of the TM CoM velocity as a function of the time of impact, while the cyan curves are obtained propagating the impact model parameter uncertainties. The plot shows that, depending on the combination of axial and lateral motion of the plunger at the retraction of the tip, a different velocity may be imparted to the TM depending on the impact time. It is possible to notice that the in-flight velocity intersects the predicted velocity at different time instants. The first intersection is identified as the estimated time of impact resulting from the analysis of the x axis. The same analysis is performed on the other axes, resulting in 6 time values for each in-flight test. The error bars are computed propagating the uncertainties of the parameters of the GPRM and impact models parameters, as shown in Fig. 11c.

The statistical compatibility of the time of impact estimated on the different axes is analyzed. Since 11 reliable non-compliant in-flight releases are available for TM1 (Bortoluzzi et al., 2021c), the overall compatibility is explored by means of a Tukey's range test (Tukey, 1949). In this formulation, each velocity component can be considered as a ”treatment” while the corresponding estimated impact time instants as ”observations” (11 in total, see Fig. 12 for all 66 estimated impact time instant).

The test compares the means of every treatment to the mean of every other treatment, allowing to find means that are statistically different from each other. The test's null hypothesis states that all the means being compared come from the same normal distribution. Given two means to be compared μ_a and μ_b, the test formula is:

$$q_{ab} = \frac{\mu_a - \mu_b}{\sqrt{\frac{mse}{n}}} \tag{9}$$

where mse is the mean squared error within the treatments and n is the number of observations per treatment. The two means are significantly different at level α if q_{ab} is larger than the critical value $q_{(k,df,\alpha)}$ obtained from the studentized range distribution, where k and df correspond to the number of treatments (i.e. 6) and the number of degrees of freedom (i.e. 60) respectively.

In the case under analysis, all the configurations between two different axes ($\mu_x = \mu_y, \ldots$) are tested as possible μ_a and μ_b. Setting α equal to 0.01 (Papoulis, 1990; Montgomery and Runger, 2010), the null hypothesis is not rejected for every means being compared. Therefore, it is possible to state that the estimated collision time instants come from the same distribution and the plunger-TM impact hypothesis is valid.

4.2. Risk-reduction strategies for the impact at the retraction

The validated model is used to explore possible design improvements to reduce the risk of impacts between the plunger and the TM at the tip retraction.

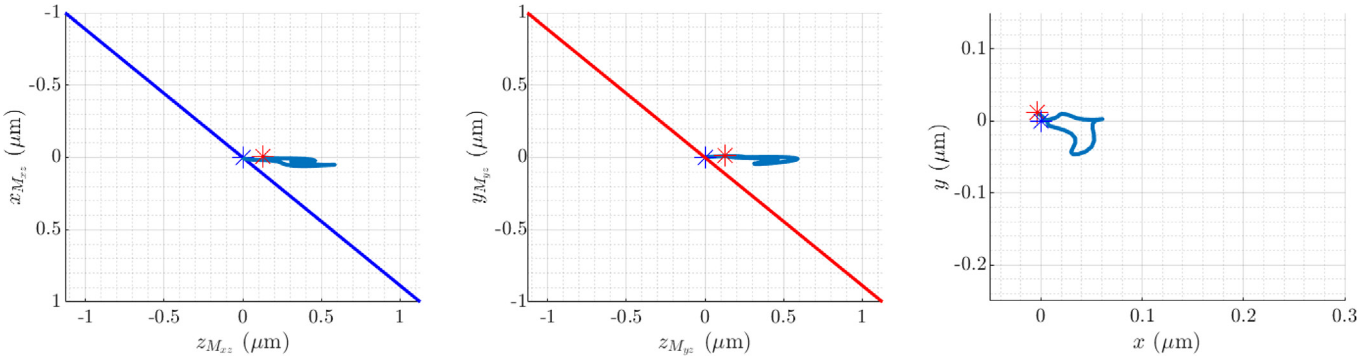

Fig. 13. Trajectory of M_{xz} projected on the x–z plane (left) and of M_{yz} on the y–z plane (middle). Trajectory of the tip edge projected on the x–y plane (right). The axes are centered in the initial position.

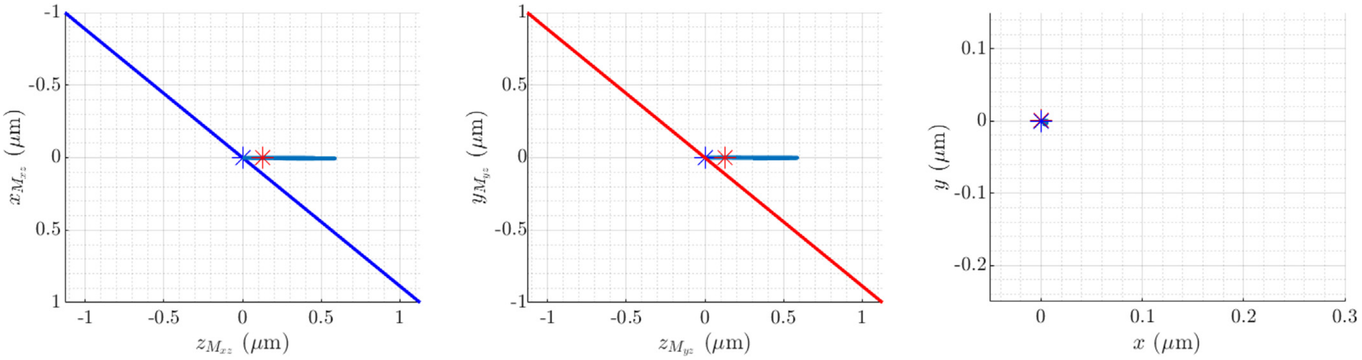

Fig. 14. Trajectory of M_{xz} projected on the x–z plane (left) and of M_{yz} on the y–z plane (middle). Trajectory of the tip edge projected on the x–y plane (right). The axes are centered in the initial position.

The first strategy consists of activating the Piezo 1. In this case, the predicted trajectories of the plunger contact points are shown in Fig. 13. As expected, the plunger develops smaller vibrations at the tip retraction with respect to the activation of Piezo 2. The ratios between the overshoot reached by the middle points on the blue and red lines using Piezo 2 and Piezo 1 in the x, y and z direction are equal to 4.0, 6.4 and 3.8 respectively.

The second strategy, whose results are shown in Fig. 14, consists of reducing the mechanism eccentricities (i.e. v_2, g_2, ρ and γ) by a factor 10 together with the activation of Piezo 1.

In this case, the lateral displacement are reduced of an order of magnitude (ratios equal to 40.0, 64.6 respectively), while the axial motion is basically unaffected.

Obviously, the reduction of the amplitude of the mechanism vibration should be compared with the available plunger-TM gap. The latter, starting from a nominal value, is eroded by manufacturing tolerances, misalignments, integration errors, etc. which are not known a priori. However, the dynamic model here described may be adopted to set requirements for the mechanism design, manufacturing, assembly and integration strategies aimed at reducing the risk of impacts at the in-flight activation of the release mechanism.

5. Conclusions and future works

In the LISA Pathfinder mission, the mechanism in charge of releasing a test mass to free-fall experienced an unexpected behavior, observed through large and unpredicted velocity components of the released object. These velocities are explained considering that impacts between the TM and the mechanism end effector (plunger) occurred at its activation. Starting from this evidence, this work aims at developing a 3D lumped parameter electro-mechanical model of the mechanism, following a completely analytical approach and validating it through an extended experimental testing campaign. The experimental campaign aims at characterising the mechanism vibrations triggered by its activation by means of the interferometric measurement of the displacement of several points along different directions. The symbolic model of the mechanism is used to provide the signals which are simultaneously fitted to the data, giving the estimation of the model parameters. An optimization technique based on the Levenberg-Marquardt algorithm is used and the model accuracy is evaluated discussing its representativeness in terms of TM kinetic energy and related impact dynamics. The results returned by the minimization algorithm are used to estimate the trajectory of the mechanism end effector at the tip retraction. The ground-based validated model, together with an impact model, is used to fully describe the in-flight dynamics of the TM release. The combination between these models and the in-flight telemetry allows to estimate the TM state at the release giving a reliable interpretation of some of the anomalies in the TM release dynamics observed in-flight.

Following the validation of the impact hypothesis, a refinement of the proposed approach will consider the axial and the lateral vibration of the linear runner and possible multiple impacts between the bodies. As a further development of the interpretation of the in-flight anomaly, the analysis will be extended to the identification of the critical conditions which produced the unexpected interaction between plunger and TM. The focus will be on the plunger to TM gap, which could have been reduced in flight by misalignments between the two plungers, arising from possible out of nominal plunger trajectories during the preparatory phases of the release (i.e. grabbing, positioning, handover). The measurement and fitting of the tip motion (i.e. μ_4) could be also included in the model. This development would lead to the refinement of the results since it allows to take into consideration the preload contact force between the tip and TM. Finally, the application of advanced uncertainty and error analysis methods (such as Yang et al., 2024c; Yang et al., 2024b; Yang et al., 2024a) could be explored according to the availability of increased number of test data.

Declaration of Competing Interest

The authors declare that they have no known competing financial interests or personal relationships that could have appeared to influence the work reported in this paper.

Acknowledgments

The authors wish to thank the LISA Pathfinder collaboration for the support throughout this work. This research is financially supported by ESA (European Space Agency), ASI (Italian Space Agency, Grant No. 2017–29-H.1–2020 ”Attività per la fase A della missione LISA”), INFN (National Institute for Nuclear Physics).

Appendix A. GPRM electro-mechanical model

The nine linearized differential equations described in Section 3 are reported in the following. In particular, Eqs. (A.1)–(A.8) refer to the lagrangian formulation applied to the generalized coordinate $z_{lr}(t), z_A(t), x_A(t), y_A(t), \eta(t), \theta(t), \mu_3(t)$ and $\mu_4(t)$ respectively, while Eq. A.9 refers to the Kirchoff law applied to the commanding circuit of Piezo 2 (see Fig. 5).

$$\begin{aligned}
&g_2m_2\theta''(t) - h_4m_4\sin(\gamma)\eta''(t) + h_4m_4\cos(\gamma)\sin(\rho)\theta''(t) + k_{lr}z_{lr}(t) + m_1z''_{lr}(t) + \dots\\
&-m_2v_2\eta''(t) + m_2z''_A(t) + m_2z''_{lr}(t) + m_3\cos(\gamma)\cos(\rho)\mu''_3(t) + m_3z''_A(t) + m_3z''_{lr}(t) + \dots\\
&+m_4\cos(\gamma)\cos(\rho)\mu''_4(t) + m_4z''_A(t) + m_4z''_{lr}(t) = 0
\end{aligned} \tag{A.1}$$

$$\begin{aligned}
&g_2m_2\theta''(t) - h_4m_4\sin(\gamma)\eta''(t) + h_4m_4\cos(\gamma)\sin(\rho)\theta''(t) + k_{A,z}z_A(t) - m_2v_2\eta''(t) + \dots\\
&+m_2z''_A(t) + m_2z''_{lr}(t) + m_3\cos(\gamma)\cos(\rho)\mu''_3(t) + m_3z''_A(t) + m_3z''_{lr}(t) + \dots\\
&+m_4\cos(\gamma)\cos(\rho)\mu''_4(t) + m_4z''_A(t) + m_4z''_{lr}(t) = 0
\end{aligned} \tag{A.2}$$

$$\begin{aligned}
&c_{A,x}d_1\eta'(t) + c_{A,x}x'_A(t) + c_{B,x}d_1\eta'(t) + c_{B,x}d_2\eta'(t) + c_{B,x}x'_A(t) + d_1k_{A,x}\eta(t) + \dots\\
&+d_1k_{B,x}\eta(t) + d_2k_{B,x}\eta(t) + h_2m_2\eta''(t) + h_3m_3\eta''(t) + h_3m_4\eta''(t) + \dots\\
&+h_4m_4\cos(\gamma)\cos(\rho)\eta''(t) + k_{A,x}x_A(t) + k_{B,x}x_A(t) + m_2x''_A(t) + \dots\\
&m_3\sin(\gamma)\mu''_3(t) + m_3x''_A(t) + m_4\sin(\gamma)\mu''_4(t) + m_4x''_A(t) = 0
\end{aligned} \tag{A.3}$$

$$\begin{aligned}
&-a_1c_{C,y}\theta'(t) - a_1c_{D,y}\theta'(t) - a_1k_{C,y}\theta(t) - a_1k_{D,y}\theta(t) - a_2c_{D,y}\theta'(t) - a_2k_{D,y}\theta(t) + \dots\\
&c_{C,y}y'_A(t) + c_{D,y}y'_A(t) - h_2m_2\theta''(t) - h_3m_3\theta''(t) - h_3m_4\theta''(t) + \dots\\
&-h_4m_4\cos(\gamma)\cos(\rho)\theta''(t) + k_{C,y}y_A(t) + k_{D,y}y_A(t) + m_2y''_A(t) + \dots\\
&+m_3\cos(\gamma)\sin(\rho)\mu''_3(t) + m_3y''_A(t) + m_4\cos(\gamma)\sin(\rho)\mu''_4(t) + m_4y''_A(t) = 0
\end{aligned} \tag{A.4}$$

$$\begin{aligned}
&\tfrac{1}{2}\left(2c_{A,x}d_1\left(d_1\eta'(t) + x'_A(t)\right) + 2c_{B,x}(d_1+d_2)\left((d_1+d_2)\eta'(t) + x'_A(t)\right)\right) - m_2v_2z''_A(t) + \dots\\
&+d_1^2k_{B,x}\eta(t) + 2d_1d_2k_{B,x}\eta(t) + d_1k_{A,x}x_A(t) + d_1k_{B,x}x_A(t) + d_2^2k_{B,x}\eta(t) + d_2k_{B,x}x_A(t) + \dots\\
&-g_2m_2v_2\theta''(t) + h_2^2m_2\eta''(t) + h_2m_2x''_A(t) - h_2m_2\eta(t)z''_{lr}(t) + h_3^2m_3\eta''(t) - m_2v_2z''_{lr}(t) + \dots\\
&+h_3^2m_4\eta''(t) + 2h_3h_4m_4\cos(\gamma)\cos(\rho)\eta''(t) + h_3m_3\sin(\gamma)\mu''_3(t) + h_3m_3x''_A(t) + \dots\\
&-h_3m_3\eta(t)z''_{lr}(t) + h_3m_4\sin(\gamma)\mu''_4(t) + h_3m_4x''_A(t) - h_3m_4\eta(t)z''_{lr}(t) + m_2v_2^2\eta''(t) + \dots\\
&+\tfrac{1}{4}h_4^2m_4\cos^2(\gamma)\cos^2(\rho)\eta''(t) - \tfrac{1}{4}h_4^2m_4\sin^2(\gamma)\cos^2(\rho)\eta''(t) - \tfrac{1}{4}h_4^2m_4\cos^2(\gamma)\sin^2(\rho)\eta''(t) + \dots\\
&+\tfrac{1}{4}h_4^2m_4\sin^2(\gamma)\eta''(t) - \tfrac{1}{4}h_4^2m_4\cos^2(\gamma)\eta''(t) - h_4^2m_4\sin(\gamma)\cos(\gamma)\sin(\rho)\theta''(t) + \dots\\
&+\tfrac{1}{4}h_4^2m_4\sin^2(\rho)\eta''(t) + \tfrac{1}{4}h_4^2m_4\cos^2(\rho)\eta''(t) + \tfrac{3}{4}h_4^2m_4\eta''(t) + h_4m_4\cos(\gamma)\cos(\rho)x''_A(t) + \dots\\
&-h_4m_4\sin(\gamma)z''_A(t) + h_4m_4\cos(\gamma)\cos(\rho)\eta(t)z''_{lr}(t) - h_4m_4\sin(\gamma)z''_{lr}(t) + J_2\eta''(t) + \dots\\
&-m_3\sin(\gamma)\mu_3(t)z''_{lr}(t) - m_4\sin(\gamma)\mu_4(t)z''_{lr}(t) + \tfrac{1}{4}h_4^2m_4\sin^2(\gamma)\sin^2(\rho)\eta''(t) = 0
\end{aligned} \tag{A.5}$$

$$\begin{aligned}
&a_1^2k_{C,y}\theta(t) + a_1^2k_{D,y}\theta(t) + \tfrac{1}{2} + 2a_1a_2k_{D,y}\theta(t) - a_1k_{C,y}y_A(t) - a_1k_{D,y}y_A(t) + \dots\\
&-\left(2c_{D,y}(a_1+a_2)\left(y'_A(t) - (a_1+a_2)\theta'(t)\right) - 2a_1c_{C,y}\left(y'_A(t) - a_1\theta'(t)\right)\right) + a_2^2k_{D,y}\theta(t) + \dots\\
&-a_2k_{D,y}y_A(t) + g_2^2m_2\theta''(t) - g_2m_2v_2\eta''(t) + g_2m_2z''_A(t) + g_2m_2z''_{lr}(t) + h_2^2m_2\theta''(t) + \dots\\
&-h_2m_2y''_A(t) - h_2m_2\theta(t)z''_{lr}(t) + h_3^2m_3\theta''(t) + h_3^2m_4\theta''(t) + 2h_3h_4m_4\cos(\gamma)\cos(\rho)\theta''(t) + \dots\\
&-h_3m_3\cos(\gamma)\sin(\rho)\mu''_3(t) - h_3m_3y''_A(t) - h_3m_3\theta(t)z''_{lr}(t) - h_3m_4\cos(\gamma)\sin(\rho)\mu''_4(t) + \dots\\
&-h_3m_4y''_A(t) - h_3m_4\theta(t)z''_{lr}(t) - h_4^2m_4\sin(\gamma)\cos(\gamma)\sin(\rho)\eta''(t) - \tfrac{1}{2}h_4^2m_4\sin^2(\gamma)\theta''(t) + \dots\\
&+\tfrac{1}{2}h_4^2m_4\cos^2(\gamma)\theta''(t) + \tfrac{1}{2}h_4^2m_4\theta''(t) - h_4m_4\cos(\gamma)\cos(\rho)y''_A(t) + h_4m_4\cos(\gamma)\sin(\rho)z''_A(t) + \dots\\
&-h_4m_4\cos(\gamma)\cos(\rho)\theta(t)z''_{lr}(t) + h_4m_4\cos(\gamma)\sin(\rho)z''_{lr}(t) + J_2\theta''(t) + \dots\\
&+m_3\cos(\gamma)\sin(\rho)\mu_3(t)z''_{lr}(t) + m_4\cos(\gamma)\sin(\rho)\mu_4(t)z''_{lr}(t) = 0
\end{aligned} \tag{A.6}$$

$$\begin{aligned}
&\tfrac{c_1C_a\mu'_3(t) + c_3C_a\mu'_3(t) - c_3C_a\mu'_4(t) + T_{em}^2\mu_3(t)}{C_a} - \tfrac{T_{em}q(t)}{C_a} + h_3m_3\sin(\gamma)\eta''(t) + \dots\\
&-h_3m_3\cos(\gamma)\sin(\rho)\theta''(t) + 2k_3\mu_3(t) - k_3\mu_4(t) + m_3\mu''_3(t) + m_3\sin(\gamma)x''_A(t) + \dots\\
&+m_3\cos(\gamma)\sin(\rho)y''_A(t) + m_3\cos(\gamma)\cos(\rho)z''_A(t) - m_3\sin(\gamma)\eta(t)z''_{lr}(t) + \dots\\
&+m_3\cos(\gamma)\sin(\rho)\theta(t)z''_{lr}(t) + m_3\cos(\gamma)\cos(\rho)z''_{lr}(t) = 0
\end{aligned} \tag{A.7}$$

$$\begin{aligned}
&c_3\left(\mu'_4(t) - \mu'_3(t)\right) + h_3m_4\sin(\gamma)\eta''(t) - h_3m_4\cos(\gamma)\sin(\rho)\theta''(t) - k_3\mu_3(t) + k_3\mu_4(t) + \dots\\
&+k_4\mu_4(t) + m_4\mu''_4(t) + m_4\sin(\gamma)x''_A(t) + m_4\cos(\gamma)\sin(\rho)y''_A(t) + m_4\cos(\gamma)\cos(\rho)z''_A(t) + \dots\\
&-m_4\sin(\gamma)\eta(t)z''_{lr}(t) + m_4\cos(\gamma)\sin(\rho)\theta(t)z''_{lr}(t) + m_4\cos(\gamma)\cos(\rho)z''_{lr}(t) = 0
\end{aligned} \tag{A.8}$$

$$RC_aq'(t) + q(t) - T_{em}\mu_3(t) - C_aV(t - t_0) = 0 \tag{A.9}$$

Appendix B. Plunger-TM impact dynamics

The solution to the system of Equations describing the impact dynamics is reported in the following. The subscripts A and B identify the two colliding bodies.

$$\begin{cases} I_T &= 0 \\ I_N &= \frac{2m_A m_B I_{A,g} I_{B,g}\left(-v^i_{A,y}+v^i_{B,y}+x_A\omega^i_A-x_B\omega^i_B\right)}{m_A x_A^2 m_B I_{B,g}+m_A m_B x_B^2 I_{A,g}+(m_A+m_B)I_{A,g}I_{B,g}} \\ V^f_N &= v^i_{A,y}-v^i_{B,y}-x_A\omega^i_A+x_B\omega^i_B \\ V^i_N &= v^i_{A,y}-v^i_{B,y}-x_A\omega^i_A+x_B\omega^i_B \\ v^f_{A,x} &= v^i_{A,x} \\ v^f_{A,y} &= \frac{I_{A,g}\left(-m_B I_{B,g}\left(v^i_{A,y}-2\left(v^i_{B,y}+x_A\omega^i_A-x_B\omega^i_B\right)\right)+m_A I_{B,g} v^i_{A,y}+m_A m_B x_B^2 v^i_{A,y}\right)+m_A x_A^2 m_B I_{B,g} v^i_{A,y}}{m_A x_A^2 m_B I_{B,g}+m_A m_B x_B^2 I_{A,g}+(m_A+m_B)I_{A,g}I_{B,g}} \\ \omega^f_A &= \frac{I_{B,g}\left(m_B\omega^i_A i_{A,g}+m_A x_A m_B\left(2v^i_{A,y}-2v^i_{B,y}-x_A\omega^i_A+2x_B\omega^i_B\right)+m_A\omega^i_A I_{A,g}\right)+m_A m_B x_B^2\omega^i_A I_{A,g}}{m_A x_A^2 m_B I_{B,g}+m_A m_B x_B^2 I_{A,g}+(m_A+m_B)I_{A,g}I_{B,g}} \\ v^f_{B,x} &= v^i_{B,x} \\ v^f_{B,y} &= \frac{I_{A,g}\left(m_A I_{B,g}\left(2v^i_{A,y}-v^i_{B,y}-2x_A\omega^i_A+2x_B\omega^i_B\right)+m_A m_B x_B^2 v^i_{B,y}+m_B I_{B,g} v^i_{B,y}\right)+m_A x_A^2 m_B I_{B,g} v^i_{B,y}}{m_A x_A^2 m_B I_{B,g}+m_A m_B x_B^2 I_{A,g}+(m_A+m_B)I_{A,g}I_{B,g}} \\ \omega^f_B &= \frac{I_{A,g}\left(m_A\omega^i_B I_{B,g}+m_A m_B x_B\left(-2v^i_{A,y}+2v^i_{B,y}+2x_A\omega^i_A-x_B\omega^i_B\right)+m_B\omega^i_B \mathrm{I}_{B,g}\right)+m_A x_A^2 m_B\omega^i_B I_{B,g}}{m_A x_A^2 m_B I_{B,g}+m_A m_B x_B^2 I_{A,g}+(m_A+m_B)I_{A,g}I_{B,g}} \end{cases} \tag{B.1}$$

where, for body k (with $k \in \{A, B\}$), $I_{k,g}$ is the moment of inertia of body k computed with respect to its center of mass, m_k is the mass, x_k, y_k are the coordinates of the body center of mass in the collision reference frame, $v_{k,x}, v_{k,y}$ are the linear velocity components, ω_k is the angular velocity of the body, V_N the normal relative velocity, and I_T I_N are the impulse tangential and normal to the colliding surfaces respectively.

References

Adriaens, H., De Koning, W.L., Banning, R., 2000. Modeling piezoelectric actuators. IEEE/ASME Trans. Mechatr. 5 (4), 331–341.

Akhan, A.F., Cojocaru, D., Marghitu, D.B., 2023. Kinetic energy for the frictional impact of two link chain. Int. J. Impact Eng. 179, 104655.

Armano, M., Audley, H., Auger, G., et al., 2017. Capacitive sensing of test mass motion with nanometer precision over millimeter-wide sensing gaps for space-borne gravitational reference sensors. Phys. Rev. D 96 (6), 062004.

Armano, M., Benedetti, M., Bogenstahl, J., et al., 2009. LISA Pathfinder: the experiment and the route to LISA. Class. Quantum Grav. 26 (9), 094001, Https://doi.org/10.1088/0264-9381/26/9/094001.

Bard, Y., 1974. Nonlinear parameter estimation. Technical Report.

Benedetti, M., Bortoluzzi, D., Baglivo, L., et al., 2011. An optimal two-input approach for impulse measurements in the nanoN···range produced by contact forces. Mech. Syst. Signal Process. 25 (5), 1646–1660, Https://doi.org/10.1016/j.ymssp.2010.11.016.

Bortoluzzi, D., Armano, M., Audley, H., et al., 2016. Injection of a body into a geodesic: Lessons learnt from the LISA Pathfinder case. In: 43rd Aerospace Mechanisms Symposium (AMS).

Bortoluzzi, D., Baglivo, L., Benedetti, M., et al., 2009. LISA Pathfinder test mass injection in geodesic motion: status of the on-ground testing. Class. Quantum Gravity 26 (9), 094011, Https://doi.org/10.1088/0264-9381/26/9/094011.

Bortoluzzi, D., Benedetti, M., Baglivo, L., et al., 2010. A new perspective in adhesion science and technology: testing dynamic failure of adhesive junctions for space applications. Exp. Mech. 50 (8), 1213–1223, Https://doi.org/10.1007/s11340-009-9327-5.

Bortoluzzi, D., Benedetti, M., Conklin, J.W., 2013. Indirect measurement of metallic adhesion force as a function of elongation under dynamic conditions. Mech. Syst. Signal Process. 38 (2), 384–398, Https://doi.org/10.1016/j.ymssp.2013.01.019.

Bortoluzzi, D., Carbone, L., Cavalleri, A., et al., 2004. Measuring random force noise for LISA aboard the LISA Pathfinder mission. Class. Quantum Gravity 21 (5), S573, Https://doi.org/10.1088/0264-9381/21/5/028.

Bortoluzzi, D., Conklin, J.W., Zanoni, C., 2013. Prediction of the LISA-Pathfinder release mechanism in-flight performance. Adv. Space Res. 51 (7), 1145–1156, Https://doi.org/10.1016/j.asr.2012.11.001.

Bortoluzzi, D., Dalla Ricca, E., 2023. Analytical–experimental characterization of metallic adhesion impulses. Tribol. Int. 177, 107974.

Bortoluzzi, D., Dalla Ricca, E., Vignotto, D. et al., 2021a. Testing of the impact dynamics of the lisa pathfinder release mechanism. In: 19th Euro. Space Mechanisms & Tribology Symp. (ESMATS).

Bortoluzzi, D., De Cecco, M., Vitale, S., et al., 2008. Dynamic measurements of impulses generated by the separation of adhered bodies under near-zero gravity conditions. Exp. Mech. 48 (6), 777–787.

Bortoluzzi, D., Foulon, B., Marirrodriga, C.G., et al., 2010. Object injection in geodesic conditions: In-flight and on-ground testing issues. Adv. Space Res. 45 (11), 1358–1379, Https://doi.org/10.1016/j.asr.2010.01.023.

Bortoluzzi, D., Mäusli, P.A., Antonello, R., et al., 2011. Modeling and identification of an electro-mechanical system: the LISA grabbing positioning and release mechanism case. Adv. Space Res. 47 (3), 453–465, Https://doi.org/10.1016/j.asr.2010.09.004.

Bortoluzzi, D., Vignotto, D., Dalla Ricca, E., et al., 2021b. Investigation of the in-flight anomalies of the lisa pathfinder test mass release mechanism. Adv. Space Res. 68 (6), 2600–2615. https://doi.org/10.1016/j.asr.2021.04.050.

Bortoluzzi, D., Vignotto, D., Zambotti, A., et al., 2021c. In-flight testing of the injection of the lisa pathfinder test mass into a geodesic. Adv. Space Res. 67 (1), 504–520, Https://doi.org/10.1016/j.asr.2020.09.009.

Bortoluzzi, D., Vignotto, D., Zambotti, A., et al., 2019. Analysis of the in-flight injection of the LISA-Pathfinder test-mass into a geodesic. In: 18th Euro. Space Mechanisms & Tribology Symp. (ESMATS).

Bortoluzzi, D., Zambotti, A., Favia, N., 2020. A vibration mode-based adhesion impulse characterization technique. Mech. Syst. Signal Process. 145, 106952, Https://doi.org/10.1016/j.ymssp.2020.106952.

Bortoluzzi, D., Zanoni, C., Conklin, J.W., 2017. On-ground testing of the role of adhesion in the LISA-Pathfinder test mass injection phase. Adv. Space Res. 59 (10), 2572–2582, Https://doi.org/10.1016/j.asr.2017.02.030.

Bortoluzzi, D., Zanoni, C., Vitale, S., 2015. Improvements in the measurement of metallic adhesion dynamics. Mech. Syst. Signal Process. 52, 600–613, Https://doi.org/10.1016/j.ymssp.2014.06.002.

Brach, R.M., 1989. Rigid body collisions. J. Appl. Mech.

Dalla Ricca, E., Bortoluzzi, D., Zanoni, C., 2024. An improved vibration multi mode-based technique for the characterization of metallic adhesion impulses. AIAA J., 1–11

Dolesi, R., Bortoluzzi, D., Bosetti, P., et al., 2003. Gravitational sensor for LISA and its technology demonstration mission. Class. Quantum Gravity 20 (10), S99, Https://doi.org/10.1088/0264-9381/20/10/312.

Draper, N.R., Smith, H., 1998. Applied regression analysis, volume 326. John Wiley & Sons.

Gavin, H.P., 2019. The levenberg-marquardt algorithm for nonlinear least squares curve-fitting problems. In: Department of Civil and Environmental Engineering. Duke University, pp. 1–19.

Khandelwal, A., Mukherjee, R., 2024. Spatial variation of the coefficient of restitution for frictionless impacts on circular beams. J. Appl. Mech. 91 (1).

Köker, I., Rozemeijer, H., Stary, F., et al., 2013. Alignment and Testing of the GPRM as Part of the LTP Caging Mechanism. In: In 15th Euro. Space Mechanisms & Tribology Symp. (ESMATS).

Kool, J., Parker, J., 1988. Analysis of the inverse problem for transient unsaturated flow. Water Resour. Res. 24 (6), 817–830, Https://doi.org/10.1029/WR024i006p00817.

Lin, J., Qi, C., Gao, F., et al., 2023. Modeling and verification for a three-degree-of-freedom flexure-based planar parallel micro manipulator. J. Mech. Robot. 15 (4), 041006.

Madsen, K., Nielsen, H.B., Tingleff, O., 2004. Methods for non-linear least squares problems.

Marquardt, D.W., 1963. An algorithm for least-squares estimation of nonlinear parameters. J. Soc. Industr. Appl. Math. 11 (2), 431–441, Https://doi.org/10.1137/0111030.

Mäusli, P., Romano, R., Lips, K. et al., 2007. GPRM-Design description. ESA internal document S2-HTS-DDD-3001, ESA.

Montgomery, D.C., Runger, G.C., 2010. Applied statistics and probability for engineers. John wiley & sons.

Neukom, A., Romano, R., Nellen, P.M., 2009. Testing and lessons learnt of LISA GPRM. In: 13th Euro. Space Mechanisms & Tribology Symp. (ESMATS).

Papoulis, A., 1990. Probability and statistics. Prentice-Hall Inc..

Schleicher, A., Ziegler, T., Schubert, R., et al., 2018. In-orbit performance of the LISA Pathfinder drag-free and attitude control system. CEAS Space J. 10 (4), 471–485, Https://doi.org/10.1007/s12567-018-0204-x.

Šimænek, J., Hopmans, J.W., 2020. 1.7 parameter optimization and nonlinear fitting. Methods of Soil Anal. Part 4: Phys. Methods 20, 139, Https://doi.org/10.2136/sssabookser5.4.c7.

Standard, I., 1988. IEEE standard on piezoelectricity. ANSI/IEEE Std, 176–1987.

Tukey, J.W., 1949. Comparing individual means in the analysis of variance. Biometrics, 99–114.

Wagner, B.J., Gorelick, S.M., 1986. A statistical methodology for estimating transport parameters: Theory and applications to one-dimensional advectivec-dispersive systems. Water Resour. Res. 22 (8), 1303–1315.

Wolfram, S., 2003. The Mathematica Book, Wolfram Research Inc. Cambridge Univ. Press, Cambridge.

Yang, C., Fan, Z., Lu, W., et al., 2024a. Uncertain iterative optimal attitude control method for periodic satellite with reliability constraint. IEEE Trans. Aerosp. Electron. Syst.

Yang, C., Fan, Z., Xia, Y., 2024b. Convex model-based reduced-order model for uncertain control systems. IEEE Trans. Syst., Man, Cybernet.: Syst.

Yang, C., Fang, Z., Ren, H., et al., 2024c. Interval uncertainty-oriented impedance force control for space manipulator with time-dependent reliability. Acta Astronaut.

Yue, Y., Gao, F., Zhao, X., et al., 2010. Relationship among input-force, payload, stiffness, and displacement of a 6-dof perpendicular parallel micromanipulator. Journal of Mechanisms and Robotics 2 (1).

Zabuga, A., 2016. Modeling the collision with friction of rigid bodies. Int. Appl. Mech. 52 (5), 557–562, Https://doi.org/10.1007/s10778-016-0776-0.

Zanoni, C., Bortoluzzi, D., 2014. Experimental-analytical qualification of a piezoelectric mechanism for a critical space application. IEEE/ASME Trans. Mechatron. 20 (1), 427–437.

Zanoni, C., Bortoluzzi, D., Conklin, J.W., et al., 2015. Summary of the results of the LISA-Pathfinder Test Mass release. J. Phys: Conf. Ser. 610 (1), 012022, Https://doi.org/10.1088/1742-6596/610/1/012022.